

EFFECTS OF ROTATION ON STELLAR SPECTRA

by

Aaron Gillich

A Thesis Submitted to Saint Mary's University, Halifax, Nova Scotia in Partial Fulfillment of the
Requirements for the Degree of

MASTER OF SCIENCE

in

Astronomy

(Department of Physics and Astronomy)

August 16, 2007, Halifax, Nova Scotia

© Aaron Gillich, 2007

Approved: Dr. Robert Deupree
Supervisor

Approved: Dr. Ian Short
Examiner

Approved: Dr. David Turner
Examiner

Date: August 16, 2007



Library and
Archives Canada

Bibliothèque et
Archives Canada

Published Heritage
Branch

Direction du
Patrimoine de l'édition

395 Wellington Street
Ottawa ON K1A 0N4
Canada

395, rue Wellington
Ottawa ON K1A 0N4
Canada

Your file *Votre référence*
ISBN: 978-0-494-35769-9
Our file *Notre référence*
ISBN: 978-0-494-35769-9

NOTICE:

The author has granted a non-exclusive license allowing Library and Archives Canada to reproduce, publish, archive, preserve, conserve, communicate to the public by telecommunication or on the Internet, loan, distribute and sell theses worldwide, for commercial or non-commercial purposes, in microform, paper, electronic and/or any other formats.

The author retains copyright ownership and moral rights in this thesis. Neither the thesis nor substantial extracts from it may be printed or otherwise reproduced without the author's permission.

AVIS:

L'auteur a accordé une licence non exclusive permettant à la Bibliothèque et Archives Canada de reproduire, publier, archiver, sauvegarder, conserver, transmettre au public par télécommunication ou par l'Internet, prêter, distribuer et vendre des thèses partout dans le monde, à des fins commerciales ou autres, sur support microforme, papier, électronique et/ou autres formats.

L'auteur conserve la propriété du droit d'auteur et des droits moraux qui protègent cette thèse. Ni la thèse ni des extraits substantiels de celle-ci ne doivent être imprimés ou autrement reproduits sans son autorisation.

In compliance with the Canadian Privacy Act some supporting forms may have been removed from this thesis.

Conformément à la loi canadienne sur la protection de la vie privée, quelques formulaires secondaires ont été enlevés de cette thèse.

While these forms may be included in the document page count, their removal does not represent any loss of content from the thesis.

Bien que ces formulaires aient inclus dans la pagination, il n'y aura aucun contenu manquant.


Canada

CONTENTS

CONTENTS	ii
LIST OF FIGURES	iv
LIST OF TABLES	viii
ACKNOWLEDGEMENTS	ix
ABSTRACT	1
1 INTRODUCTION	2
1.1 BACKGROUND	2
1.2 MODELLING ROTATING STARS	4
1.2.1 INTERIOR STRUCTURES AND VON ZEIPPEL'S LAW	5
1.2.2 ATMOSPHERES, SEDs, AND LINES	8
1.3 PRESENT WORK	10
2 THE CODES	15
2.1 ROTORC	15
2.2 PHOENIX	17
2.3 THE INTENSITY INTEGRATOR CODE - CLIC	22
2.3.1 SED MODE	22
2.3.2 LINE MODE	24
3 INCLINATION CURVES	26
3.1 SPECTRAL ENERGY DISTRIBUTIONS	26
3.2 INCLINATION CURVES	27

CONTENTS

iii

3.2.1	UNIFORM ROTATION	35
3.2.2	DIFFERENTIAL ROTATION	38
3.2.3	VON ZEIPEL COMPARISON	42
4	LINE PROFILES	46
4.1	EFFECTS OF DIFFERENTIAL ROTATION	46
4.2	VON ZEIPEL'S LAW	59
5	CONCLUSIONS	64
	REFERENCES	67

LIST OF FIGURES

- 1.1 Theoretical H-R diagram for three families of models. The dotted lines connect models of equal rotational velocities. The abscissa denotes a mean value of T_e taken over the visible surface weighted by $I(3646+)$. Reproduced with permission from Collins & Harrington (1966). 12
- 3.1 PHOENIX plane parallel spectra for models from $T_{eff} = 20000$ K to 34000 K at $\log g = 3.4$ (top) and $\log g = 4.3$ (bottom) showing dependence of spectra on effective gravity. Flux is given at the surface of the star. 28
- 3.2 Output from CLIC code. Flux at Earth from 40 pc for 10 inclinations from pole to equator for $12M_{\odot}$ star uniformly rotating with $v = 500$ km s $^{-1}$. The range in spectra is similar to that shown in Fig. 3.1, which implies a significant range in effective temperature from pole to equator. 29
- 3.3 Flux bands used for ratios A (solid) and B (dotted), shown with spectra for $T_{eff} = 20000$ and 34000 K and $\log g = 3.4$ and 4.3 representing the four corners of the grid. 31
- 3.4 Flux ratios A and B as functions of temperature for both $\log g = 3.4$ and 4.3 . Horizontal dotted lines give the flux ratios for the model being determined. The vertical dot-dash line represents the final calculated T_{eff} and $\log g$ for the rotating SED. . . 33
- 3.5 Inclination curves for uniformly rotating $12 M_{\odot}$ models at $v = 255$ - 575 km s $^{-1}$. Note that critical rotation is approximately 600 km s $^{-1}$. ZAMS models at 11 , 12 , $13 M_{\odot}$ are given for scale, show that a uniform rotation rate of only 255 km s $^{-1}$ can shift a star's apparent location by up to the equivalent of a solar mass. 34

3.6	Selected inclination curves from Fig. 3.5 given with error bars. Uncertainties in luminosity increased with decreasing luminosity, while uncertainties in temperature increased with increasing temperature.	36
3.7	13 inclination curves calculated for $12 M_{\odot}$ uniformly rotating stars from $v = 0$ to 575 km s^{-1} . As the distance between points increases, the curves become less linear. Note that the most significant changes are evident when the star is viewed nearly equator-on, where the star becomes much cooler.	37
3.8	Rotational velocity curves showing each inclination as a function of velocity. Models are the same as for Fig. 3.7.	39
3.9	Inclination curves for $10 M_{\odot}$ models differentially rotating at $v = 120 \text{ km s}^{-1}$ with β increasing from 0 to 2. Non-rotating 9, 10, and $11 M_{\odot}$ models are shown for scale. Differential rotation makes the star appear to be rotating much more rapidly than it is if one assumed uniform rotation.	40
3.10	Inclination curves for $10 M_{\odot}$ models differentially rotating at $v = 240 \text{ km s}^{-1}$ with β increasing from 0 to 1.2. Non-rotating 9, 10, and $11 M_{\odot}$ models are shown for scale. Smaller differences in β have a smaller, but still distinctive effect on the inclination curve.	41
3.11	Differences between ROTORC and von Zeipel temperature profiles for $12 M_{\odot}$ models with increasing uniform rotation velocities. The differences become significant for rotational velocities above about 350 km s^{-1}	43
3.12	Differences between integrated ROTORC and von Zeipel model fluxes for $v = 500 \text{ km s}^{-1}$, for $12 M_{\odot}$ models at $i = 0, 30, 60,$ and 90° . Flux is given at Earth from a distance of 40 pc. As shown in the temperature differences of Fig. 3.11 the differences between ROTORC and von Zeipel model become more pronounced at the equator.	44

3.13 ROTORC vs. von Zeipel model inclination curves for $12 M_{\odot}$ uniformly rotating models. The differences between them exceed the uncertainties for any rotational velocity greater than around 350 km s^{-1}	45
4.1 Surface rotation velocity as a function of colatitude for various rotation profiles. All models are $10 M_{\odot}$ and have surface rotational velocities of 120 km s^{-1} . The most significant differences in rotation profiles occur between colatitudes of 10° and 60° . .	48
4.2 CII $\lambda 4268$ doublet for a $10 M_{\odot}$ model viewed equator on. It is a commonly seen view demonstrating the effects of differential rotation on line profiles.	49
4.3 He I $\lambda 4923$ and O II $\lambda 4926$ for $10 M_{\odot}$ non-rotating model.	51
4.4 He I $\lambda 4923$ for a $10 M_{\odot}$ model rotating at 120 km s^{-1} . Top: $i=0^{\circ}$, middle: $i=10^{\circ}$, bottom: $i=20^{\circ}$. Note that the wavelength scale is constant but the flux scale varies from Figs. 4.4 to 4.6.	52
4.5 He I $\lambda 4923$ for a $10 M_{\odot}$ model rotating at 120 km s^{-1} . Top: $i=30^{\circ}$, middle: $i=40^{\circ}$, bottom: $i=50^{\circ}$	53
4.6 He I $\lambda 4923$ for a $10 M_{\odot}$ model rotating at 120 km s^{-1} . Top: $i=60^{\circ}$, middle: $i=70^{\circ}$, bottom: $i=90^{\circ}$	54
4.7 $H\delta$ profiles for a $10 M_{\odot}$ model rotating at 120 km s^{-1} , Top: $i=30^{\circ}$, middle: $i=60^{\circ}$, bottom: $i=90^{\circ}$	55
4.8 He I $\lambda 4923$ profiles for a $10 M_{\odot}$ rotating at 240 km s^{-1} Top: $i=30^{\circ}$, middle: $i=60^{\circ}$, bottom: $i=90^{\circ}$	57
4.9 $H\delta$ profiles for a $10 M_{\odot}$ rotating at 240 km s^{-1} , Top: $i=30^{\circ}$, middle: $i=60^{\circ}$, bottom: $i=90^{\circ}$	58
4.10 HeI $\lambda 4923$ for $10 M_{\odot}$ model rotating at 120 km s^{-1} . Top: $i=30^{\circ}$, bottom: $i=60^{\circ}$. . .	60
4.11 He I $\lambda 4923$ generated from ROTORC (solid) and Von Zeipel (dotted) structures for uniformly rotating $12 M_{\odot}$ models viewed equator on.	61

4.12 H δ generated from ROTORC (solid) and Von Zeipel (dotted) structures for uniformly rotating 12 M $_{\odot}$ models viewed equator on.	63
---	----

LIST OF TABLES

- 2.1 List of species treated in non-LTE. Number of energy levels and line transitions included for each ionization stage are given. Note that only a subset of the total species that PHOENIX is capable of treating in non-LTE is listed. 20
- 3.1 ROTORC model file describing surface of $12 M_{\odot}$ star uniformly rotating with $v=500$ km s^{-1} 27

ACKNOWLEDGEMENTS

I would first like to thank my supervisor, Dr. Robert Deupree for his considerable advice, guidance, and patience. I would also like to thank Dr. Ian Short. Without his support I would never have had the opportunity to do this work. I owe him a further thanks for his extensive help with PHOENIX and modelling atmospheres. I would also like to thank Dr. Joris van Bever for his contributions at our bi-weekly research meetings, and Catherine Lovekin for her help with her code CLIC. Thank you to Nathalie Toque for providing a series of differentially rotating stellar structure models. Thank you as well to Dr. Ian Short and Dr. David Turner for being on my defense committee.

Next I would like to thank my wonderful fiancée Lucía. This has been a two year commitment from both of us, and I truly could not have done it without you. I would also like to thank Tomomi, Jon, Nick, Catherine, Chris, Dan, Jon, and Joel. For the past two years you have all been there with advice, support, and laughter, in whichever order they were needed.

ABSTRACT

Effects of Rotation on Stellar Spectra

by Aaron Gillich

Abstract: Models have been produced to study the spectral energy distributions (SEDs) and absorption lines for rapidly rotating B stars. A fully implicit 2D stellar structure and evolution code was used to generate the rotating structure models. The code PHOENIX was then used to generate non-LTE stellar atmospheres and spectra. An integrator code, CLIC, then created SEDs and absorption lines as viewed from 10 inclination angles. The SEDs were used to create a series of inclination curves, defining a rotating star's possible positions on an HR diagram. It was found that uniform rotation creates a relatively straight line parallel to the main sequence. The line extends in length and moves away from the main sequence as the rate of rotation increases. Differential rotation creates a more extended and complex inclination curve. The effects of differential rotation on line profiles was explored. It was found that differential rotation creates a very different profile from uniform rotation, especially when viewed closer to the pole. Both the SEDs and line profiles were used to test the limits of von Zeipel's theorem against more realistic models. The SEDs produced appreciably different inclination curves for rotation rates greater than around 0.76 of critical rotation. The difference in the line profiles produced by von Zeipel's models and the more realistic models were small.

August 16, 2007

CHAPTER 1

INTRODUCTION

The nature of rotating stars has long been studied by stellar theorists, yet continues to be a very elusive problem. Many of the tools, both observational and computational, that are used to analyze non-rotating stars become less useful when rotation is included. As I will discuss, rotation not only introduces a series of new questions, but complicates a number of older ones as well. Everything from a star's internal structure, its evolution, its chemical composition, and even its position on the HR diagram become challenging questions to answer when the star is rotating sufficiently rapidly. Some new dilemmas introduced by rotation include determining the velocity at which it is rotating, determining the angular momentum distribution, and assessing how these factors affect the other properties of the star.

1.1 BACKGROUND

There are many different fronts from which the problem of rotating stars can be addressed. This work will focus on computational modelling and building synthetic spectra for rotating stars. Much of what is known about both rotating and non-rotating stars has come from models. Stellar evolution codes can create detailed models of a star's structure. This can give the pressure, density, and temperature distributions inside the star, as well as at its surface as it evolves. Stellar atmosphere codes can solve the equation of radiative transfer to give synthetic spectra for a star. This can be used to reproduce observables like a spectral energy distribution (SED), or individual spectral lines. The procedure is relatively straightforward in the case of non-rotating stars, but becomes significantly more complex when the star is rotating. I will therefore begin by outlining the key considerations in modelling rotation, such as velocity determination and rotation laws, followed by giving a history

of how these problems have been confronted in the past and what tools have been developed to overcome them. Finally I will introduce the present work and what it will be contributing to our knowledge of rotating stars.

A non-rotating star can, with a few basic assumptions, be modelled as a sphere, with the effective temperature and gravity constant everywhere on the surface. While the fundamental physics do not change when the star is rotating, several new variables are introduced.

As a star rotates, the centrifugal force stretches the star away from the rotation axis. This creates an oblate shape that does not emit flux equally at all locations on the surface. The flux leaving at the poles will be greater than the flux leaving at the equator, and the flux seen from a rotating star will vary depending on the inclination (i), the angle between the observer's line of sight and the rotation axis, where $i = 0^\circ$ represents the pole-on view and $i = 90^\circ$ represents the equator-on view.

One must also consider how to determine observationally whether a star is rotating. The method for determining the rotation velocity of a star comes from analyzing individual spectral lines. As a star rotates, the light coming from the advancing and receding sides will be Doppler shifted, symmetrically broadening the line profile. Comparing a broadened line with an unbroadened one can therefore reveal the rotation rate that is observed for the star. The angle of inclination is unknown, therefore, only a component of the velocity is observed, which is expressed as $v \sin i$. Early type stars are frequently rapid rotators, with $v \sin i$ as high as 400 km s^{-1} (Slettebak, 1949). As the rotation rate increases, a spectral line will become broader and flatter as the wavelengths of light that create the line are shifted further away from line center. However, for rotational effects alone, the equivalent width, W_λ , of the line stays the same. If a star is rotating sufficiently rapidly, some key lines can be broadened so much that they become indiscernible. This can make abundances, temperatures, and even the rotational velocity itself difficult to determine.

Not only is the rotation rate as defined by the surface equatorial velocity important in determining observed features, but so is the internal angular momentum distribution. Stellar rotation laws can be divided into two main categories, conservative and non-conservative. A conservative rotation

law is any for which the force can be written as a gradient of the potential (Tassoul, 1978). A non-conservative rotation law might be one in which the angular velocity varied with both colatitude and distance from the rotation axis. Conservative rotation laws allow more mathematical simplifications and flexibility, and are far more frequently modelled. All the rotation laws considered in this thesis are conservative.

The only star for which the internal angular momentum distribution is even partially known is the Sun. Models of any other star must, therefore, have a rotation profile applied to them ad hoc. For a conservative rotation law, the star must be either rotating as a solid body or differentially rotating. In solid body, i.e. uniform, rotation the angular velocity is constant throughout the star, whereas for conservative differential rotation the angular velocity varies with distance from the rotation axis. One example of a differential rotation law has the angular velocity increasing with the distance from the rotation axis. This is the way in which the Sun rotates (Schou *et al.*, 1998; Thompson, 2003), and will hereafter be referred to as increasing differential rotation. Another example of differential rotation is that in which the angular velocity decreases with distance from the rotation axis. This type will hereafter be referred to as decreasing differential rotation. Smith (1971) argued based on observations of the Praesepe and Hyades clusters that uniform rotation is likely unrealistic, but because of large uncertainties no particular non-uniform rotation law can be specified. More recent studies, as I will discuss, have only slightly improved on this idea. Given the lack of knowledge, uniform rotation laws are still frequently modelled because of their relative simplicity.

1.2 MODELLING ROTATING STARS

The modelling of the spectra of rotating stars can be treated with three distinct computational steps: the calculation of the interior stellar structure, the calculation of the atmosphere based on that structure, and then from those the calculation of the SEDs and line profiles. While this paper will primarily study the effects of rotation on the two observables, the SEDs and absorption lines,

the benefits of proper structure calculations will be discussed as well. It has been shown that the effects of rotation on the interior structure play a significant role in determining the emergent spectra (Collins *et al.*, 1991). This section gives a brief history and evolution of the ideas behind modelling both rotating stellar structures and atmospheres, and the ways in which they have been used to create synthetic SEDs and line profiles for rotating stars.

1.2.1 INTERIOR STRUCTURES AND VON ZEIPEL'S LAW

It is well understood that rotation distorts the shape of a star, making it asymmetrical. Such stars can still be treated as a one dimensional problem if certain conditions are met. Most calculations of the stellar structure of rotating stars rely on calculating an equipotential surface, along which density, pressure, and temperature are constant. Note that this will only be possible for conservative rotation laws. The problem can then be treated as 1D with the equipotential surface being the independent variable. Determining the location of the equipotentials as functions of r and θ then becomes a more manageable 2D aspect of the problem. While the nuances and methods have evolved significantly, this is the fundamental idea behind most modelling of rotating stars. Some more recent efforts make the considerable step of treating more elements of the problem in 2D.

The method of using an equipotential to describe the effects of rotation on stellar structure dates back to von Zeipel (1924). He designed a mathematical approach to treating rotating stellar masses, showing that in hydrostatic equilibrium, surfaces of constant total potential are also surfaces of constant pressure and density. From the ideal gas law, if pressure and density are constant across an equipotential surface then temperature must be as well. For a purely radiative star the flux can be expressed as the product of the temperature gradient and a radiative conductivity. This in turn means that for a purely radiative star, the flux is constant on an equipotential surface as well ($F \propto \nabla\Phi$). The flux at the surface is proportional to T_{eff}^4 , which leads to the proportionality, $T_{eff} \propto g_{eff}^{1/4}$, where T_{eff} is the effective temperature and g_{eff} is the effective gravity at the surface. The total potential for a rotating star is the sum of the gravitational potential and the rotational potential. By

defining the gravitational contribution at the surface as a Roche potential and specifying a radius somewhere on the star (usually the equator), one can then solve for $R(\theta)$ everywhere on the surface of the star.

This then allows the effective gravity to be found from,

$$g_{eff} = -\frac{GM}{R(\theta)^2} + \omega^2 R(\theta) \sin^2 \theta \quad (1.1)$$

where G is the gravitational constant, M is the mass, ω is the angular velocity, and θ is the colatitude. This in turn allows one to get T_{eff} , with the constant of proportionality usually determined by setting the total flux to be some desired value.

It is a very common tool used for simplifying the calculation of a rotating stellar structure. It provides a relatively simple way to determine the inputs for a stellar atmosphere calculation, T_{eff} and g_{eff} , as they would appear at a given colatitude, θ , for a given rotation velocity, ω .

As computational capabilities evolved, the law was used very extensively for a number of diverse purposes. Sweet & Roy (1953) built models that treated rotation as a first order perturbation. Their approach could only handle slow rotation, and was improved upon by Roxburgh *et al.* (1965), who studied rapid rotation by dividing the star into two different sections. The interior section was designed to contain the bulk of the mass and hence the gravitational potential, so that the contribution of the exterior section to the potential could be given by an approximate solution to Laplace's equation. Sackmann & Anand (1970) improved these models by incorporating radiation pressure.

These methods treat the problem as 1D perpendicular to equipotential surfaces. That was sufficient provided that the star was uniformly rotating. To handle more diverse angular momentum distributions, such as differential rotation, Ostriker & Mark (1968) developed the self consistent field method (SFC). They divide the problem into two independent steps, solving for the density distribution and the total potential, then iterating to converge to a solution. Jackson (1970) expanded the

idea to include the Henyey method, a powerful technique for solving systems of nonlinear differential equations. While Ostriker and Mark considered only barytropic stars, the Jackson method solves the full set of stellar structure equations.

Another method for describing rotating stars was developed by Clement (1974, 1978, 1979), who solved Poisson's equation in two dimensions simultaneously with the equations of thermal and mechanical equilibrium using a finite difference technique. The method avoided the usual double series expansion for the gravitational potential, but was only valid for conservative rotation laws.

All of the above methods offer ways to solve the internal structure of a rotating star. While some newer methods allow for a 2D treatment, the vast majority of stellar structure models today still make use of the 1D treatment of equipotential surfaces offered by von Zeipel's law and solve for a Roche potential at the surface. There are, however, several shortcomings implicit in the method. The first is the assumption that the surface of the star can be represented as a Roche potential. It assumes that the mass is sufficiently concentrated towards the centre, which for uniformly rotating stars is a good assumption, but it becomes less accurate with more extreme angular momentum distributions. The next flaw arises from a contradiction in the von Zeipel model in that it does not couple the effective temperature and the surface temperature. As described, the von Zeipel model is based on the idea that the temperature is constant across an equipotential surface, yet the effective temperature clearly changes from pole to equator. That can only be true if the surface temperature and effective temperature are completely independent of one another, which should not be true (Lovekin *et al.*, 2006). The von Zeipel model predicts that the equatorial effective temperature goes to zero as the model approaches critical rotation. Some of the limitations were tested by Lovekin *et al.* (2006) in her comparison of von Zeipel models with fully 2D structure models from ROTORC (Deupree, 1990).

1.2.2 ATMOSPHERES, SEDS, AND LINES

The surface parameters generated from the rotating structure model then become inputs for the atmosphere calculation. Among the first to study rotating atmospheres was Collins (1963). As he described it, the problem of deriving the spectrum of a rotating star can be divided into two parts. The first part is to define the fundamental parameters determining a stellar atmosphere that is appropriate to the physical conditions at a given point on the surface of the star, using the structure modelling described above. The second part is to determine the atmospheric structure and the specific intensity at a given point on the surface and to integrate it over the visible hemisphere of the star. The surface properties of the visible hemisphere will vary with the angle of inclination. All methods follow these concepts.

In his initial demonstration of the idea, Collins (1963) used a structure model based on von Zeipel's law, uniform rotation, and a gray atmosphere. The gray atmosphere approximation greatly simplified the treatment of the radiative transfer equation and hence the integration of the specific intensity over the visible hemisphere of the star. He found that luminosity changed significantly, by up to a magnitude with inclination from $i = 0^\circ$ to $i = 90^\circ$. He later improved on this work (Collins, 1965) by replacing the gray atmosphere approximation with a series of model atmospheres, and found the change in luminosity to be even greater. Roxburgh & Strittmatter (1965) supported these results with similar work.

Over the years, a number of refinements were added to the process of modelling rotating atmospheres. For example, Hardorp & Strittmatter (1968a) showed that the energy transported by circulation is very small compared to the energy transported by radiation, and can thus be omitted from atmosphere calculations. Their results agreed qualitatively with Collins (1965) and Roxburgh & Strittmatter (1965). Maeder & Peytremann (1970) improved the realism of LTE atmospheres, which had thus far only included continuum opacities, by incorporating hydrogen line opacities for the Balmer and Lyman series.

With an extensive set of models, Collins *et al.* (1991), Collins (1974), and Collins & Sonneborn (1977) showed that the effects of rotation on the structure of the interior would likely play as large a role in determining the emergent spectrum as the rotational effects on the atmosphere. Slettebak *et al.* (1980) and Frémat *et al.* (2005) were among the first to create spectra of rotating stars using a series of non-LTE atmospheres. It can be stated generally that every adjustment that has increased the realism of modelling has also increased the apparent effects of rotation on the luminosity of the star.

Atmospheres are generally created with two different outputs in mind, the SED and individual line profiles. These two outputs are fundamentally connected, and while many of the refinements in modelling techniques can be applied to both, they are often treated as independent topics. It is therefore of interest to discuss some of the previously developed techniques specific to modelling line profiles.

There are two fundamentally different ways to model a rotationally broadened line profile. An atmosphere can output the specific intensity, I , emerging at any angle with respect to the surface normal from the surface of an atmosphere. One can take the component of that intensity in the direction of the observer and integrate across the surface of the star. The appropriate intensities can be Doppler shifted the appropriate amount, giving the flux for the rotationally broadened line profile.

If intensities are not available, it is also possible to estimate the line profile from a non-rotating flux spectrum, F_λ , using a limb darkening law. This method is clearly far less computationally intensive. An observed spectral absorption line can be rotationally broadened using a limb darkening law completely mathematically, without ever modelling the star at all. The idea was initially described by Carroll (1928, 1933) and Shajn & Struve (1929). They treated the star as a circular disk, with a linear limb darkening law applied uniformly to all parts of the disk. Elvey (1930) then used the results in creating the first list of rotational velocities derived by comparing observed line contours with this simplified geometric approach.

Treating the visible surface of a rotating star as a circular disk is clearly not ideal. Later studies would consider the effects of deformation at the equator, or gravitational darkening (Slettebak, 1949). Hardorp & Strittmatter (1968b) suggest that not including gravitational darkening effects could lead to underestimating $v \sin i$ by up to 40%. Collins & Truax (1995) looked at the classical treatment of rotational broadening and found that inappropriate values of limb darkening coefficients can lead to significant errors in even moderately rotating stars.

Any modelling of a rotationally broadened line profile that is generated from local surface intensities and integrated over the star will have both limb darkening and gravitational darkening automatically incorporated into the calculation. While this is a more direct way of calculating the line, as it does not require the tuning of any mathematical factors, it is much more computationally demanding. For that reason, even today, limb darkening laws are frequently employed to calculate rotationally broadened line profiles. All the work presented here however, is done by direct numerical integration of the intensities.

1.3 PRESENT WORK

The goal of this thesis is to establish by improved methodology to what extent observables like SEDs and spectral absorption lines hold clues describing a star's rotation. As discussed in the previous section, this problem has been explored for decades; however the sophistication of our models allows a more realistic treatment than previous approaches. This section introduces the improvements made on previous ideas, and describes the work that was done with both SEDs and spectral line profiles.

The results presented in this thesis were generated using three computational tools. The rotating stellar structure models come from a fully implicit 2D stellar evolution code, ROTORC, eliminating the need to make simplifying assumptions using von Zeipel's theorem. The atmospheres come from the atmosphere and spectrum synthesis code PHOENIX, which is capable of handling an

unprecedented number of elements and atomic energy levels in non-LTE. The code, CLIC, combines the results of these tools by interpolating among a grid of plane parallel atmospheres and integrating the intensities over the surface of the star to produce a series of detailed and realistic spectra for rapidly rotating stars.

The SED for a rapidly rotating star appears approximately similar to that of a non-rotating star. However, a key idea is that the SED for a rotating star is affected by the angle from which it is being observed. Non-rotating stars have a luminosity and effective temperature that do not change with the inclination of the observer, allowing them to be represented as unique points on the HR diagram. For rotating stars, however, the luminosity and effective temperature deduced from observations depends on the angle of inclination to the rotation axis. Therefore, rotating stars should appear on the theoretical HR diagram not as points, but as curves, with the angle of inclination as the free parameter. This will hereafter be referred to as an inclination curve. A principal goal of this work is to define the inclination curve and show how it changes with rotation velocity and rotation profile.

For decades the techniques described in the previous section were applied to the question of a rotating star's position on the HR diagram. Roxburgh & Strittmatter (1965) used a Roche model and gray atmospheres to estimate the effect of uniform rotation on broadening the main sequence. Collins (1966), Collins & Harrington (1966), and Hardorp & Strittmatter (1968a) expanded the result with non-gray LTE atmospheres based on the interior structure models of Roxburgh *et al.* (1965). Bodenheimer (1971) worked with differentially rotating models based on the methods of Ostriker & Mark (1968) and Jackson (1970). The results all agreed qualitatively, and are demonstrated in Fig. 1.1, which is taken from Collins & Harrington (1966). This represents an example of an earlier version of the inclination curves I present here.

These studies have been done primarily with plane parallel LTE atmospheres and 1D interior structures with surface parameters defined using von Zeipel's law. The present work takes this type of analysis a step further. I will be using detailed 2D structure models, and non-LTE plane parallel

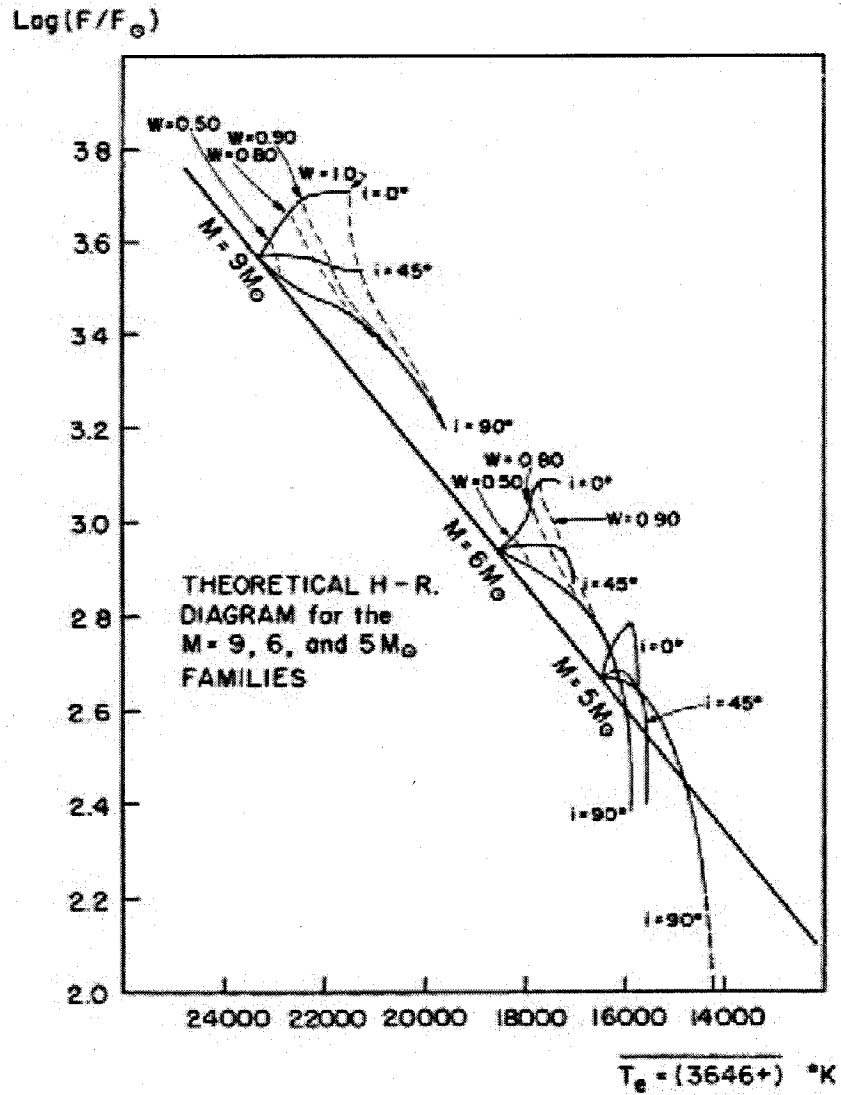


Figure 1.1: Theoretical H-R diagram for three families of models. The dotted lines connect models of equal rotational velocities. The abscissa denotes a mean value of T_e taken over the visible surface weighted by $I(3646+)$. Reproduced with permission from Collins & Harrington (1966).

atmospheres to establish inclination curves from zero to near critical uniform rotation, as well as several examples of differential rotation.

The next part of this thesis focuses on individual line profiles. Spectral absorption lines are very useful diagnostic tools that can reveal a number of things about the nature of a star, such as its temperature, luminosity, composition, and rotation velocity. As discussed, a comparison of a broadened line with an unbroadened one can reveal the rotation rate of the star. The next challenge is then to determine what else the broadening can tell us about the rotation. I will take a closer look at the dependence of an absorption line on the rotation law of the star by comparing the results from uniform rotation with those from varying degrees of differential rotation.

One of the primary methods of determining the rotational broadening in a line profile is with mathematical treatments that use limb darkening coefficients. Huang (1961) was among the first to extend this mathematical approach to defining the effects of differential rotation on line profiles. He focused on increasing differential rotation and found that it had the effect of narrowing the line, and extending its core. Decreasing differential rotation has the opposite effect, flattening the core, and further broadening the wings.

Stoeckley (1968) proposed a method of deducing $v \sin i$, i , and the amount of differential rotation by plotting the half-widths of three different line profiles. He compared his calculations with high precision spectrometer data ($3 \text{ \AA } \text{mm}^{-1}$) taken with the Cambridge 36 inch reflector for 19 very bright early type stars. He found his uncertainties too high to make any definite conclusions, but noted that uniform rotation, or decreasing differential rotation, were likely in early type stars, as opposed to increasing differential rotation. He later supported the idea (Stoeckley & Buscombe, 1987) using non-LTE line profiles generated from a gravity darkened Roche model star.

Gray (1977) pioneered the use of Fourier transforms in analyzing line profiles and searching for differential rotation. He found that many subtleties could be revealed in the Fourier domain that would otherwise be undetectable. His approach has since been followed by Garcia-Alegre *et al.* (1982), Reiners & Schmitt (2002), Reiners (2003). Their work was done using the analytical approach

to line broadening rather than using integrated intensities, and focused primarily on increasing differential rotation.

For both the SED and line portions of this thesis, I will be focusing on decreasing differential rotation and ignoring increasing differential rotation altogether. There are several reasons for this. Despite some evidence that early type stars exhibit decreasing differential rotation, very little study has been put towards demonstrating the effects of decreasing differential rotation on spectral lines. The tendency towards modelling increasing differential rotation is understandable from an atmospheres point of view, as it is more readily observable in the Sun. However, any knowledge gained is not readily transferable to early type stars. One motivation of choosing decreasing differential rotation is therefore to help address this lack. Furthermore, increasing differential rotation takes the central parts of the star, which are already rotating slowly, and slows them down even more. It is therefore far more intriguing from a stellar structure point of view to study decreasing differential rotation.

Another subject that will be explored throughout this thesis is the applicability of von Zeipel's law. Given the extensive degree to which von Zeipel's law is used, it is very useful to quantify its limitations, for both the inclination curves and for the spectral line profiles.

CHAPTER 2

THE CODES

The goal of this work is to determine what observables like SEDs and spectral lines can tell us about a star's rotation. The previous chapter outlined the way in which such observables have typically been modelled. Both the SED and individual line profiles observed from a rotating star represent flux distributions that are the weighted sum of the intensities in the direction of the observer coming from everywhere on the visible hemisphere of the star. Because of rotation, the surface parameters of temperature and gravity, and hence intensity, vary with colatitude, and intensity coming from the surface of the star are Doppler shifted. A method is therefore needed to take the surface intensities at the appropriate temperature and gravity coming from each part of the star and integrate them over the visible surface. This calculation is done using the integrator code CLIC.

For CLIC to do the required tasks, it needs two sets of input. The first is a list of intensities at all the required angles with respect to the local surface normal as functions of effective temperature and gravity. That is provided by the atmosphere and spectrum synthesis code PHOENIX. The second piece of input CLIC requires is knowledge of the surface parameters such as effective temperature, effective gravity, radius, and rotation velocity. They come from the fully implicit 2D stellar evolution code ROTORC. The ROTORC results are also used to determine the grid of local surface parameters needed by PHOENIX. This chapter defines each of the three computational components in detail and describes the improvements offered over previous studies.

2.1 ROTORC

A 1D stellar evolution code with the aid of 2D treatments of equipotential surfaces is useful for modelling non-rotating or slowly rotating stars, however it is not clear that it can accurately model

rapidly rotating stars. Rapid rotation can significantly deform the star, and there are currently only two ways to determine its surface structure: using von Zeipel's law, or using a multi-dimensional stellar evolution code such as ROTORC (Deupree, 1990, 1995). The Jackson (1970) method presented earlier has the potential to perform 2D calculations without referring to von Zeipel's law, but it is limited by somewhat crude boundary conditions. Clement (1974, 1978, 1979) offered a 2D solution to Poisson's equation, though it was limited to conservative rotation laws so that suitably modified 1D stellar structure equations could be used.

ROTORC is therefore the only fully implicit two dimensional stellar evolution and hydrodynamics code capable of handling arbitrary rotation laws. A fully implicit time dependent calculation includes the values at the advanced time step in all terms rather than just in the time derivative terms. There are several features that provide ROTORC with more realism than a typical structure code. A 1D code handles four stellar structure equations: hydrostatic equilibrium, thermal equilibrium, the stipulation of the temperature gradient as either the adiabatic or convective temperature gradient, and mass conservation. ROTORC uses the Henyey technique to implicitly solve seven conservation equations. The equation for hydrostatic equilibrium, which in 1D cases is the conservation of momentum, becomes three independent momentum equations, which treat the r , θ , and ϕ components separately. The ϕ component is calculated, but constrained to be axisymmetric, so that technically ROTORC is a 2.5D code. ROTORC also solves Poisson's equation in two dimensions. The thermal equilibrium and temperature gradient are combined into one energy equation, and the mass conservation must be treated in 2D. Finally, the 2D hydrogen composition conservation equation must be solved implicitly for time dependent evolution.

The results from ROTORC that are required for the present work are the effective temperature, effective gravity, rotation velocity, and radius at the rotating surface. The key difference between ROTORC and other codes is that ROTORC allows them to be calculated directly from the equations described above, rather than from von Zeipel's law and a Roche potential.

The present work is concerned with analyzing the effects of rotation on the SEDs and spectral

lines of early B type stars. ZAMS models were therefore constructed for uniformly rotating $12 M_{\odot}$ (approximately B0) stars ranging in equatorial surface velocity from 0 to 575 km s^{-1} , which approaches critical rotation of about 600 km s^{-1} . Differentially rotating models were also constructed for $10 M_{\odot}$ (approximately B1) stars with a rotational velocity of 120 km s^{-1} with β ranging from $\beta = 0$ to 2, and 240 km s^{-1} with β ranging from $\beta = 0$ to 1.2, where β is controls the amount of differential rotation according to the following equation:

$$\omega(\varpi) = \frac{\omega_o}{1 + (\alpha\varpi)^\beta} \quad (2.1)$$

Here ϖ is the distance from the rotation axis, ω is the angular velocity, and ω_o and α are constants. $\beta = 0$ for uniform rotation and $\beta = 2$ for the maximum possible amount of differential rotation. ROTORC models provide the effective temperature, radius, rotation velocity, and effective gravity in ten colatitudinal zones to be used later by the integrator code CLIC, when making the SED for the rotating star.

2.2 PHOENIX

The next step in synthesizing the spectrum of a rotating star is to create a grid of non-rotating model atmospheres covering the range in T_{eff} and g_{eff} provided by the ROTORC surface structure. This grid was created using the non-LTE stellar atmosphere and spectrum synthesis code PHOENIX. The code models a stellar atmosphere by solving, among other things, the radiative transfer equation, which for a 1D, static case, using plane-parallel geometry, along a ray is:

$$\frac{dI_\lambda}{d\tau_\lambda} = I_\lambda - \frac{j_\lambda}{\kappa_\lambda}, \quad (2.2)$$

where j_λ and κ_λ are the emission and absorption coefficients, respectively, and τ_λ is the optical depth, all at wavelength, λ . The quantity j_λ/κ_λ is defined to be the source function, $S(\lambda)$.

The plane-parallel approximation means that the atmosphere is treated as a 1D semi-infinite slab such that all the parameters vary only with depth. It is a valid assumption provided the horizontal mean photon path is small compared to the horizontal distance over which the atmosphere changes, and the atmospheric thickness is far less than the star's radius. That is generally a fair assumption, as the radius of a star is so large the surface is effectively flat, and the horizon will appear the same in every direction. For a rotating star the assumption is least true at the equator, as it has lower effective gravity and the surface is more curved than anywhere else on the star. The combination of the two allows the horizontal mean photon path to be slightly greater relative to horizontal changes in the atmosphere. However, since the equator is cooler for the high rotation rates at which the curvature becomes significant, it contributes less to the integrated flux, and the effect on the SED is small.

In order to solve the equation of radiative transfer, an atmosphere code must manage thousands of energy levels for the various atomic elements. That can be done by assuming the energy levels are populated according to local thermodynamic equilibrium (LTE), or with a more realistic, but more complicated, treatment in non-LTE. In LTE, the radiation and matter are assumed to be in equilibrium with each other locally, everywhere throughout the atmosphere. The radiation, excitation, and ionization temperatures are set equal to the kinetic temperature of the gas, which allows the simplification of setting the source function to be equal to the Planck function. Energy levels are thus populated according to Maxwell-Boltzmann statistics. It is a very powerful simplification; however, LTE is known to be unrealistic in some cases (Mihalas & Athay, 1973). Non-LTE treatments overcome the assumption by decoupling the temperatures of matter and radiation. PHOENIX uses an accelerated iteration procedure to solve the coupled radiative transfer and non-LTE statistical equilibrium equations with many energy levels in non-LTE (Hauschildt & Baron, 1999).

One of the newer aspects of this work is the number of elements treated in non-LTE. Short *et al.* (1999) have greatly increased the number of species and ionization stages that can be handled in non-LTE. Non-LTE models can now be constructed with at least two ionization stages of 24

elements, and the lowest six ionization stages of the 20 most important elements, including much of the Fe group. Short *et al.* (1999) contains details of the atomic data and formulae for the various processes.

While treatment of more species in non-LTE, particularly the Fe group, has been well studied (Short & Hauschildt, 2005), the work focused on solar type stars. Different ionization stages are present in different temperature ranges, and it was found that among the cooler models, for temperatures below 24000 K, the code had trouble converging to a stable temperature structure throughout the atmosphere. From examination of the non-LTE departure coefficients, it was discovered that both silicon and phosphorus caused the lack of convergence. Therefore at 24000 K and below, every ionization stage for those two elements were treated in LTE.

Despite this adjustment, there were still some difficulties converging a temperature structure in some cooler models. Integrating the PHOENIX output flux and comparing it to the flux obtained from the Stefan-Boltzmann law,

$$F = \sigma T_{eff}^4, \quad (2.3)$$

yielded an estimate of the uncertainty caused by the inaccuracy. The error ranged to about 4%. However, a principal goal of this work is to analyze individual lines, for which the non-LTE treatment is extremely valuable.

While the errors might appear high, there are numerous advantages to a non-LTE treatment. Nature is not in LTE, and furthermore, it is known that the LTE assumption becomes less true for hotter stars (Hardorp & Strittmatter, 1968a). LTE by definition works best in a collision dominated atmosphere, however, as the temperature, and hence the radiation intensity, increase, radiative transitions become proportionally more significant. The Balmer series, for example, cannot be properly modelled in hot stars using LTE. Therefore, while the effects of non-LTE treatment on SEDs require more study, the benefits, and in particular the benefits for line calculations, still justify the non-LTE treatment for the present work. Table 2.1 shows the different species and ionization

Table 2.1: List of species treated in non-LTE. Number of energy levels and line transitions included for each ionization stage are given. Note that only a subset of the total species that PHOENIX is capable of treating in non-LTE is listed.

Element	I	II	III	IV
H	50/1225	-	-	-
He	19/37	10/45	-	-
Li	57/333	55/124	-	-
C	228/1387	85/336	79/365	-
N	252/2313	152/1110	87/266	-
O	36/66	171/1304	137/765	-
Ne	26/37	-	-	-
Na	53/142	35/171	-	-
Mg	273/835	72/340	91/656	-
Al	111/250	188/1674	58/297	31/142
Si*	329/1871	93/436	155/1027	52/292
P*	229/903	89/760	51/145	50/174
S	146/439	84/444	41/170	28/50
K	73/210	22/66	38/178	-
Ca	194/1029	87/455	150/1661	-
Fe	494/6903	620/13675	566/9721	243/2592

* Denotes elements included in non-LTE only at 26000K and above.

stages, as well as the number of energy levels and transitions, included in the rate equations. Note that only a subset of the total number of species and ionization stages that PHOENIX is capable of treating in non-LTE is listed.

PHOENIX converges to a solution if the star is in hydrostatic equilibrium. For cooler stars, the contribution of radiation pressure to the hydrostatic equilibrium equation is usually negligible and is hence omitted. For hotter stars, however, it can become relevant. At cooler temperatures the neglect is perfectly valid, however for sufficiently hot stars, stellar winds can make the hydrostatic equilibrium assumption invalid. When radiation pressure is included in the hydrostatic equilibrium equation, the gas pressure decreases to maintain the total pressure required by hydrostatic equilibrium. For temperatures greater than around 24000 K, radiation pressure becomes so large that it forces the gas pressure below zero, creating an unphysical situation and causing the code to fail. While PHOENIX is capable of modelling very diverse atmospheric conditions, the form used here simulates stable, static stellar atmospheres. The inclusion of radiatively driven stellar winds, while

possible with PHOENIX, is not of critical importance in B stars, and was beyond the scope of this work. Rather than include radiation pressure in only part of the grid below 24000 K, it was decided to eliminate radiation pressure from the models altogether.

Lanz & Hubeny (2007) built a grid of non-LTE model atmospheres covering a similar range to that used here. They also used plane parallel atmospheres in hydrostatic equilibrium. They solved the issue of radiation pressure by numerically limiting the radiative acceleration at the appropriate optical depths in order to ensure convergence of the model. They state that the model spectra are not affected by the approximation as those layers only influence strong resonance lines that form in a stellar wind.

A grid of model atmospheres was constructed from $T_{eff} = 20000\text{K}$ to 34000K at intervals of 2000K and covering a surface gravity range of $\log(g_{eff}) = 2.5$ to 4.3 at intervals of 0.3 . The intervals provide enough resolution that the integrator code can interpolate to any desired temperature with very low uncertainty, as shown in the following section. Each spectrum was calculated from 900\AA to 10000\AA at a sampling, $\Delta\lambda$, of 0.02\AA . The detailed sampling was required because the same grid of atmospheres was used to model not only the SEDs, but many individual lines as well. In addition, accurately computing a lower resolution SED requires a synthetic spectrum with fine enough sampling to critically sample individual spectral lines, which is then convolved to lower resolution. A lower limit of 900\AA was selected because there are no lines of interest below the Lyman limit, so a sampling of 0.02\AA is clearly not required. In the regions of the spectrum outside the specified range (i.e. below 900\AA and above 10000\AA), PHOENIX models any lines that are treated in non-LTE, though at a non-uniform sampling. For the stars in the hotter part of the grid, there is a non-negligible amount of flux below 900\AA that must be included in the integral of the flux, but a lower resolution is sufficient to incorporate it. An upper limit of 10000\AA was chosen because the corresponding range covers every spectral line needed, and is sufficiently far into the infrared that an analytic expression for the Rayleigh-Jeans tail can be applied seamlessly when integrated. Solar abundances of $Z = 0.02$ have been deemed appropriate for B stars (Brown *et al.*, 1986; Lennon

et al., 1990), and were thus used throughout this work.

Two different outputs from PHOENIX were used. The first is the flux spectrum, $F_\lambda(\lambda)$, which is the SED. It is the flux at every wavelength specified, with additional points for non-LTE lines where needed. The flux can be compared with the CLIC results for a spherically symmetric model. The second is a intensity spectra, $I_\lambda(\lambda)$, at the surface, sampled at every wavelength that appears in the flux spectrum. These intensities give the amount of light being emitted at 32 different angles, θ , with respect to the surface normal of the plane parallel atmosphere. It is this intensity file that the integrator code uses to evaluate the SED.

2.3 THE INTENSITY INTEGRATOR CODE - CLIC

Given the surface properties of a rotating star from ROTORC and the grid of intensity spectra from plane-parallel atmospheres covering the required range, a tool is needed to combine the two results and integrate the intensity over the surface of the star to obtain the flux seen by an observer. An atmosphere integrator code, CLIC, has been developed by Lovekin (2005). It divides the surface of the star into a 2-D mesh of 200 colatitudinal zones and 400 azimuthal zones. It reads in the ROTORC properties of the star being modelled, and interpolates among the intensity spectra to find the appropriate intensity in the direction of the observer. It does that for each zone of the mesh, then outputs the integrated flux for the rotating star as a function of inclination from pole to equator.

2.3.1 SED MODE

CLIC can be used to calculate the entire spectrum, or any part of the spectrum in SED mode. For each wavelength, the code evaluates the following expression:

$$F_\lambda = \int_{\theta} \int_{\phi} \frac{I_\lambda(\xi(\theta, \phi))}{d^2} dA_{proj} \quad (2.4)$$

where ξ is the angle between the surface normal for that zone and the observer, θ and ϕ are the colatitude and the azimuthal angles, respectively, F is the flux, I is the intensity, d is the distance to the observer, and A_{proj} is the projection of the surface area of the zone. It performs the integral for a line of sight ranging from $i = 0^\circ$ to $i = 90^\circ$ with $\Delta i = 10^\circ$.

Each wavelength in a PHOENIX model atmosphere is presented as a table of intensities at 32 different angles with respect to the surface normal, ranging from $\theta = 0^\circ$ to 180° . In order to determine a zonal contribution to the flux, the code must calculate the angle ξ between the observer and the local surface normal for that zone. Such a calculation is complicated by the oblateness of the star, as the surface normal for each zone will not pass through the star's center. From the angle ξ , the appropriate component of the intensity is taken from the PHOENIX model atmosphere at each wavelength. The process is repeated at every wavelength with the correct value of ξ for each zone in the 200 by 400 surface mesh, giving the total integrated flux for the star. The loop is then repeated for each desired inclination. The result is 10 separate integrated flux spectra showing how the spectra from a rotating star would appear as a function of inclination.

The range of models that can be calculated by CLIC is limited by the grid of non-rotating model atmospheres available. Spectra can be calculated for stars rotating at any velocity from zero up to critical rotation, provided neither the pole nor equatorial effective temperatures or gravities are outside the range of the grid. The resolution of the output spectra is limited only by the resolution of the original plane-parallel atmosphere grid.

There is one final limitation to consider. Stars that are both rapidly rotating and highly differential with points close to the rotation axis rotating far more rapidly than at larger distances from the axis can tend to expand at the equator and contract at the poles, in comparison with uniformly rotating models. If the contraction becomes significant, the star can pinch in at the poles creating a slight doughnut shape. The surface of the star will subsequently have an inflection point near the pole, and the plane parallel approximation would cease to be valid, as the horizon would not appear the same in all directions.

Because the SED covers a sufficiently large section of the spectrum, the effects of rotational broadening on individual lines are unnoticeable. The SED shows broad band effects where the width of the band is far greater than the width of a single line. As such it is unnecessary, as well as too computationally taxing, to calculate Doppler broadening for individual line profiles across the entire SED. CLIC was written to be "embarrassingly parallel", meaning that there is as little information as possible passed between the processors as infrequently as possible. For the SED calculation it is relatively straightforward since the code simply divides the spectrum into sections and passes an equal number of wavelengths to each processor. Each does its calculation and passes its portion of the spectrum back to the master processor. Each processor can handle its own group of wavelengths without any knowledge of the activities of the other processors because there is no interaction with the calculations at other wavelengths.

There are two separate sources of uncertainty to be considered for the integrated flux; the uncertainty from the integration itself and the uncertainty in interpolation between points in the PHOENIX grid. The integration itself carries an uncertainty of 0.2% tied to the resolution of the mesh. The interpolation between model atmospheres in the PHOENIX grid is linear in $\log T$ and $\log g$ and has an uncertainty of about 1% to 4%. Both of the uncertainties were found by comparing non-rotating CLIC flux spectra with flux spectra calculated directly from PHOENIX. As such, some of the uncertainty arises from the uncertainties in the PHOENIX models themselves.

2.3.2 LINE MODE

The calculation of the individual lines incorporates the Doppler broadening from the rotation. This complicates the embarrassingly parallel nature of the code because some lines are broadened to wavelengths that were sent to a different processor. In order to allow the processors to continue to act independently of one another, the code creates separate bins for the shifted wavelengths, which are then recombined into the complete flux by the master processor.

Apart from the Doppler broadening calculation, the code operates in exactly the same manner

as for the SED calculation. The output is the Doppler broadened flux spectrum, showing the line as it would appear from 10 different inclinations from pole to equator.

CHAPTER 3

INCLINATION CURVES

Rotating stars appear on the theoretical HR diagram not as points, but as curves, with the angle of inclination as the free parameter. This chapter computes inclination curves and shows how they change with rotation velocity as well as rotation profile. It is a very valuable tool when observing a rotating star. Any subsequent analysis or observation of a rotating star is contingent upon our understanding of its location on the theoretical HR diagram as a function of inclination. Many massive stars are also variable, often at several frequencies, and their frequencies can provide valuable information about the interior structure of the star. This is true only if the observable properties of the star can be related to the star's intrinsic properties. For rapidly rotating stars, the inclination curve is required to determine this relation. Work is also being done using synthetic star clusters to determine if the inclination curve can reveal anything about a star's rotation purely from its perceived location on the HR diagram.

To generate an inclination curve, several pieces of information are required. First, a SED for the entire spectrum as a function of inclination is needed, and is obtained from CLIC as described in the previous section. Next, a method is needed to deduce the luminosity and temperature from the SEDs so that they can be plotted on an HR diagram. Because the flux is calculated at 10 different inclination angles from pole on to equator on, each inclination curve is composed of ten points. One inclination curve is generated for each rotation velocity or rotation profile.

3.1 SPECTRAL ENERGY DISTRIBUTIONS

An example of a surface structure is shown in Table 3.1 for a $12 M_{\odot}$ star uniformly rotating with $v=500 \text{ km s}^{-1}$. In this instance, CLIC chooses a rectangular grid of non-rotating atmospheres

Table 3.1: ROTORC model file describing surface of $12 M_{\odot}$ star uniformly rotating with $v=500 \text{ km s}^{-1}$.

Colatitude [$^{\circ}$]	Radius [R_{\odot}]	T_{eff} [K]	$\log g$ [cgs]	Rotation Velocity [km s^{-1}]
4.5	4.284	29118.0	4.2507	30
13.5	4.319	28888.0	4.2390	899
22.5	4.388	28422.0	4.2279	149.8
31.5	4.475	28013.0	4.1816	208.6
40.5	4.597	27407.0	4.1342	266.3
49.5	4.753	26696.0	4.0712	322.4
58.5	4.961	25646.0	3.9841	377.4
67.5	5.182	24759.0	3.8785	427.2
76.5	5.427	23594.0	3.7451	470.1
85.5	5.605	22608.0	3.6243	498.5

ranging from $T_{eff} = 22000 \text{ K}$ to $T_{eff} = 30000 \text{ K}$ and from $\log g = 3.4$ to $\log g = 4.3$. A series of non-rotating spectra for increasing temperature at $\log g = 3.4$ and 4.3 is shown in Fig. 3.1. The spectrum of a star clearly changes significantly with temperature, but the spectrum is sensitive to changes in $\log g$ as well.

CLIC combines the appropriate parts of each spectrum according to equation 2.4, which scales them as they would appear from Earth at a distance being set by the user. A distance of 40 pc was used throughout this work. CLIC then outputs the spectrum of the rotating star at 10 different inclination angles, as shown in Fig. 3.2. The 10 spectra represent the flux one would observe from a $12 M_{\odot}$ star rotating uniformly at 500 km s^{-1} . Each spectrum must now be processed to determine its coordinates on an HR diagram. Each spectrum will provide one point on the inclination curve.

3.2 INCLINATION CURVES

A process must be applied to each spectrum to determine that star's luminosity and effective temperature at each of the 10 inclination angles. The bolometric luminosity, L_{bol} , is found by using the formula:

$$L = 4\pi F d^2, \quad (3.1)$$

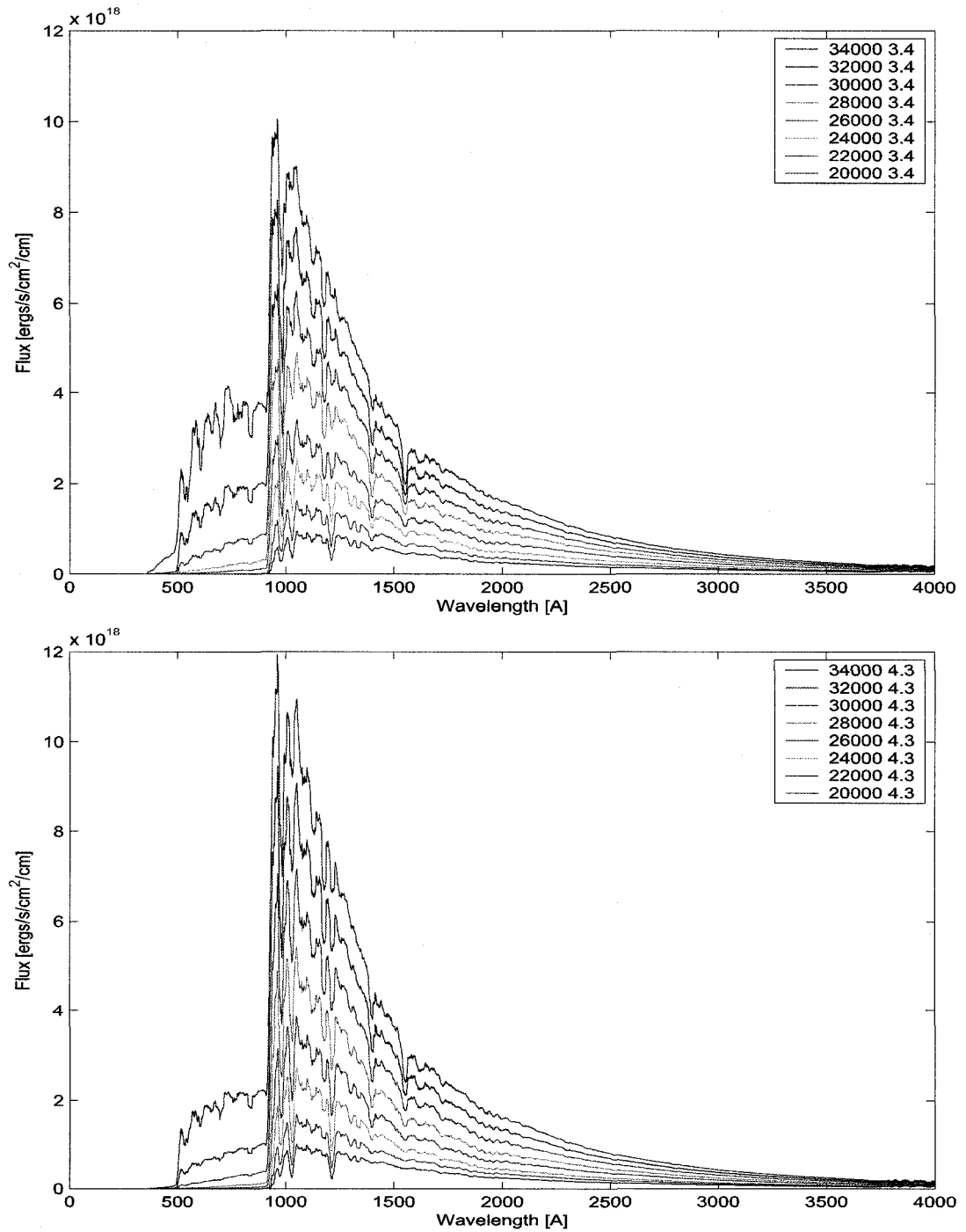


Figure 3.1: PHOENIX plane parallel spectra for models from $T_{eff} = 20000$ K to 34000 K at $\log g = 3.4$ (top) and $\log g = 4.3$ (bottom) showing dependence of spectra on effective gravity. Flux is given at the surface of the star.

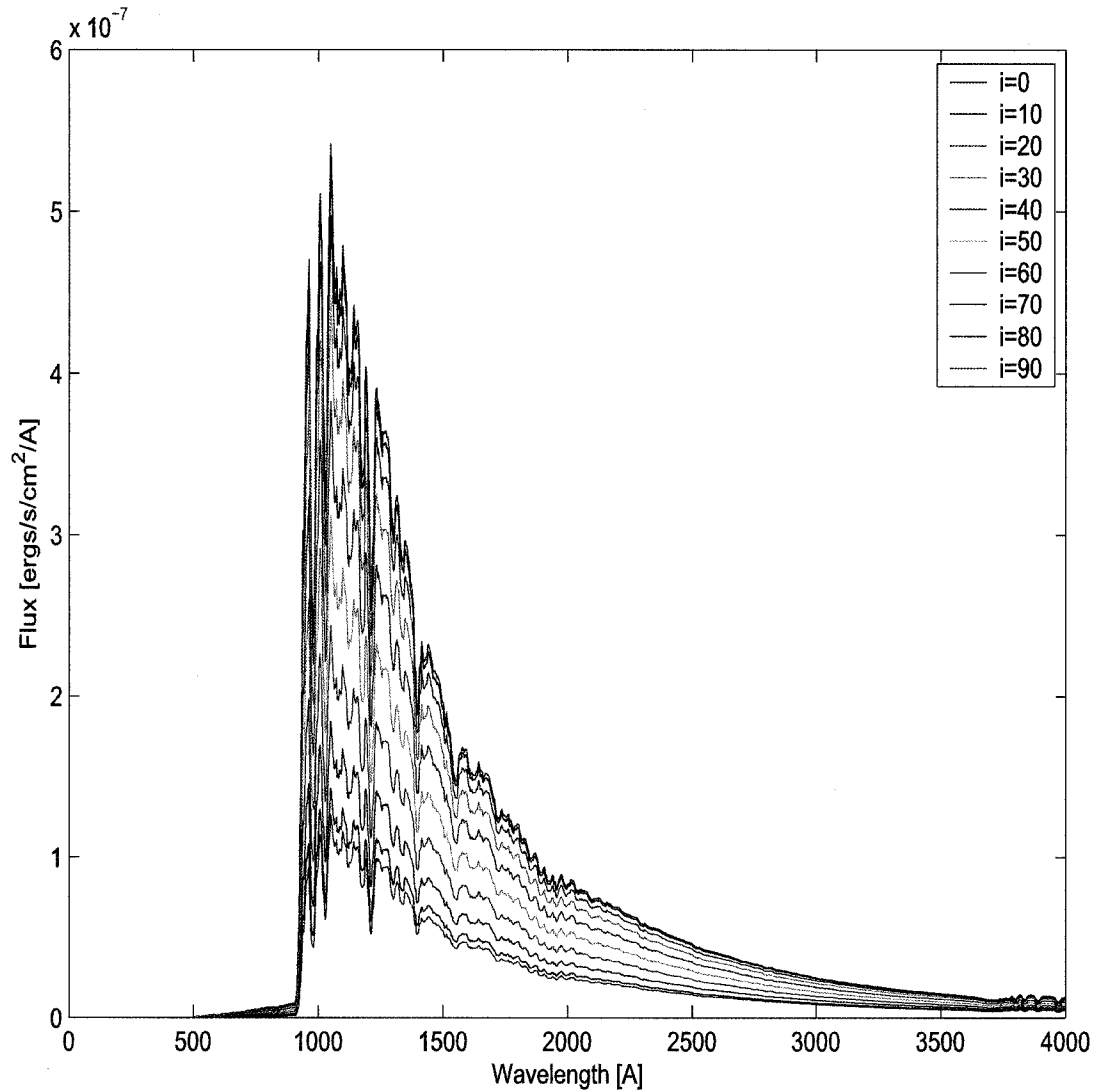


Figure 3.2: Output from CLIC code. Flux at Earth from 40 pc for 10 inclinations from pole to equator for $12M_{\odot}$ star uniformly rotating with $v = 500 \text{ km s}^{-1}$. The range in spectra is similar to that shown in Fig. 3.1, which implies a significant range in effective temperature from pole to equator.

where d is the distance to the star, and F is the bolometric flux, which is obtained by integrating the spectrum from 0 to 10000 Å then adding an analytical expression for the Rayleigh-Jeans tail. Note that L is independent of d when equations 2.4 and 3.1 are combined.

The temperature calculation is more complex. The temperature cannot simply be taken from

$$L = 4\pi R^2 \sigma T^4 \quad (3.2)$$

because for a rotating star the value of R is not constant everywhere on the star's surface. The temperature is therefore determined by taking a ratio of fluxes, i.e. colour indices, in two parts of the spectrum and then comparing it to the same flux ratios computed from a grid of flux spectra from non-rotating stars. This method is well known, and widely used. However, the presence of rotation again complicates matters. As we saw in Fig. 3.1, the spectrum is dependent on $\log g$ as well as effective temperature, so that the ratio of two fluxes does not offer a unique solution. It was necessary to use two different flux ratios to develop a relationship between the flux ratio and the effective temperature, and a separate relationship between the flux ratio and the effective gravity.

The procedure involved multiple steps. First the two flux ratios A and B were chosen. Each was the ratio of the flux in one band of the UV to the flux in a band of the visual. Ratio A compares the fluxes at 2650 Å - 2732 Å to those at 5184 Å - 5239 Å, and ratio B compares the fluxes at 1972 Å - 2054 Å to those at 5506 Å - 5575 Å. The wavelengths are somewhat flexible and were chosen to give the greatest sensitivity over the largest range of temperatures. However, because I use two flux ratios and find the intersection point of two different relationships, many different flux ratios could be used, provided that ratio A was not equal to ratio B.

In order to determine a spectrum's dependence on $\log g$, the next step was to take two sets of models of constant $\log g$ from the grid of non-rotating atmospheres at $\log g = 3.4$ and $\log g = 4.3$. Flux ratios A and B were derived for models of all eight T_{eff} values at both $\log g$ values. The four different flux ratios are plotted in Fig. 3.4 as a function of temperature. There are now two curves

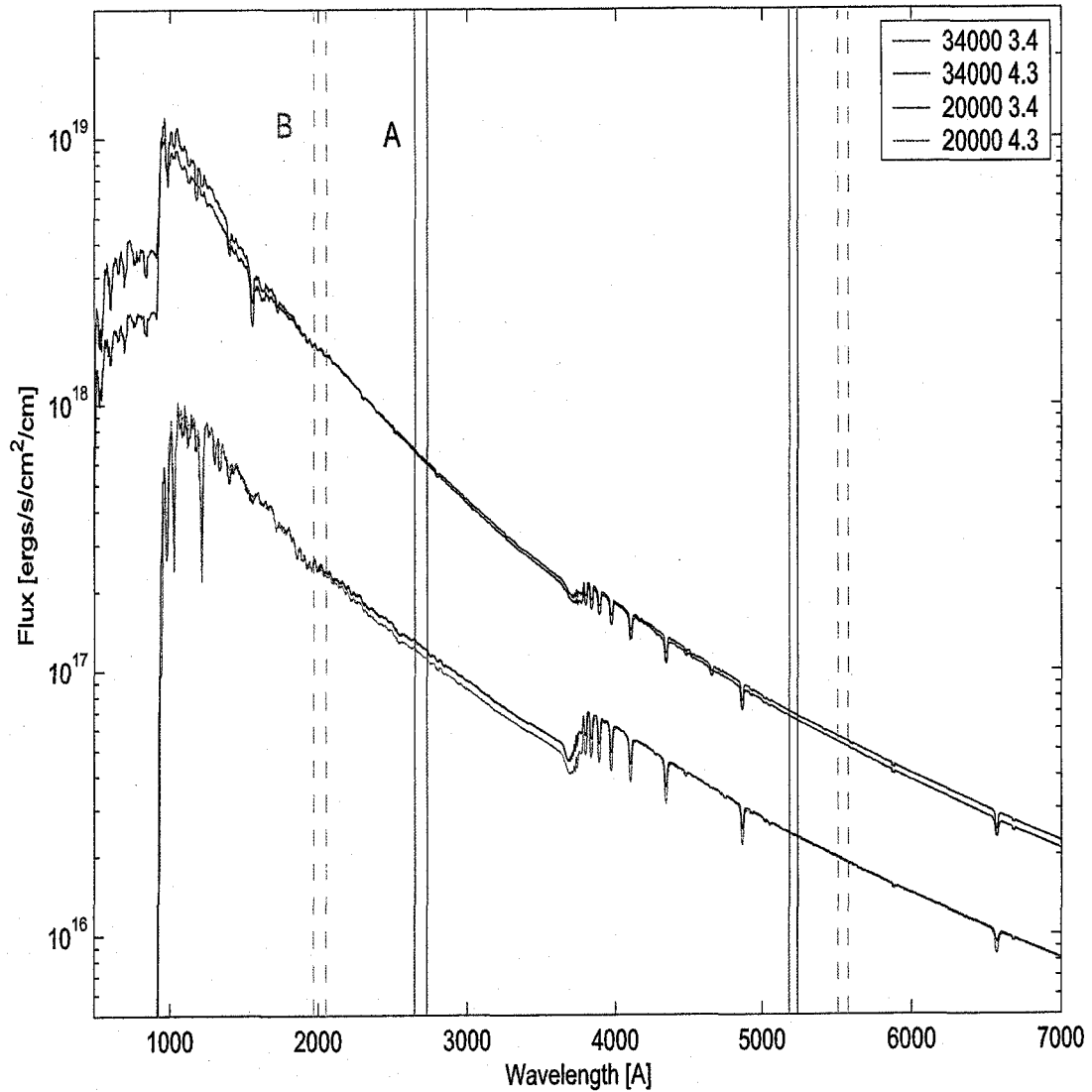


Figure 3.3: Flux bands used for ratios A (solid) and B (dotted), shown with spectra for $T_{eff} = 20000$ and 34000 K and $\log g = 3.4$ and 4.3 representing the four corners of the grid.

for each colour, one showing the change in the ratio as a function of temperature for $\log g = 3.4$ and one for $\log g = 4.3$. The true $\log g$ of the spectrum being analyzed will be linearly interpolated from the two.

The flux ratios A and B from the rotating model for which the effective temperature is being sought are shown by horizontal dotted lines. The correct temperature, shown with the vertical dot-dash line can be found by moving across the horizontal ratio lines until the value of $\log g$ determined by the interpolation is reached. It can be solved as a system of two linear equations in the unknowns T_{eff} and $\log g$. The assumption of a linear relationship was deemed to be sufficiently accurate, given that the distances between points in the grid are sufficiently small. As will be shown, the resulting uncertainties are small. If the value of $\log g$ at any inclination angle is outside the range of 3.4-4.3 the linear relationship allows extrapolation to find a solution. The $\log g$ values 3.4 and 4.3 were chosen because they cover the most significant range of $\log g$ space in the grid. Intermediate values could have been used to increase the accuracy of the interpolation, however, the linear relationship between 3.4 and 4.3 was sufficient, as the resulting uncertainties demonstrate.

With this approach, one obtains the luminosity and effective temperature for a rotating star at 10 different inclinations from pole to equator, making up one inclination curve. Fig. 3.5 shows several such curves as they would appear on the HR diagram. The increasing rate of rotation clearly makes a significant difference to the star's possible location on the HR diagram.

In assessing the uncertainties present in the method, one must consider several different sources, some of which have already been explained in detail. There will be uncertainties in the spectra themselves attributable to the difficulty of converging non-LTE models, the uncertainty from the integrator code when combining the models into a spectrum from a rotating star, and finally the uncertainties in calculating a luminosity and temperature based on that spectrum. As discussed, the errors from the PHOENIX spectra range from 0% to 4%, and the integrator code uncertainties are 0.2% for the integration and 1% to 4% for the interpolation. The uncertainties in extracting the luminosity and temperature were found by applying the method to several non-rotating stars of

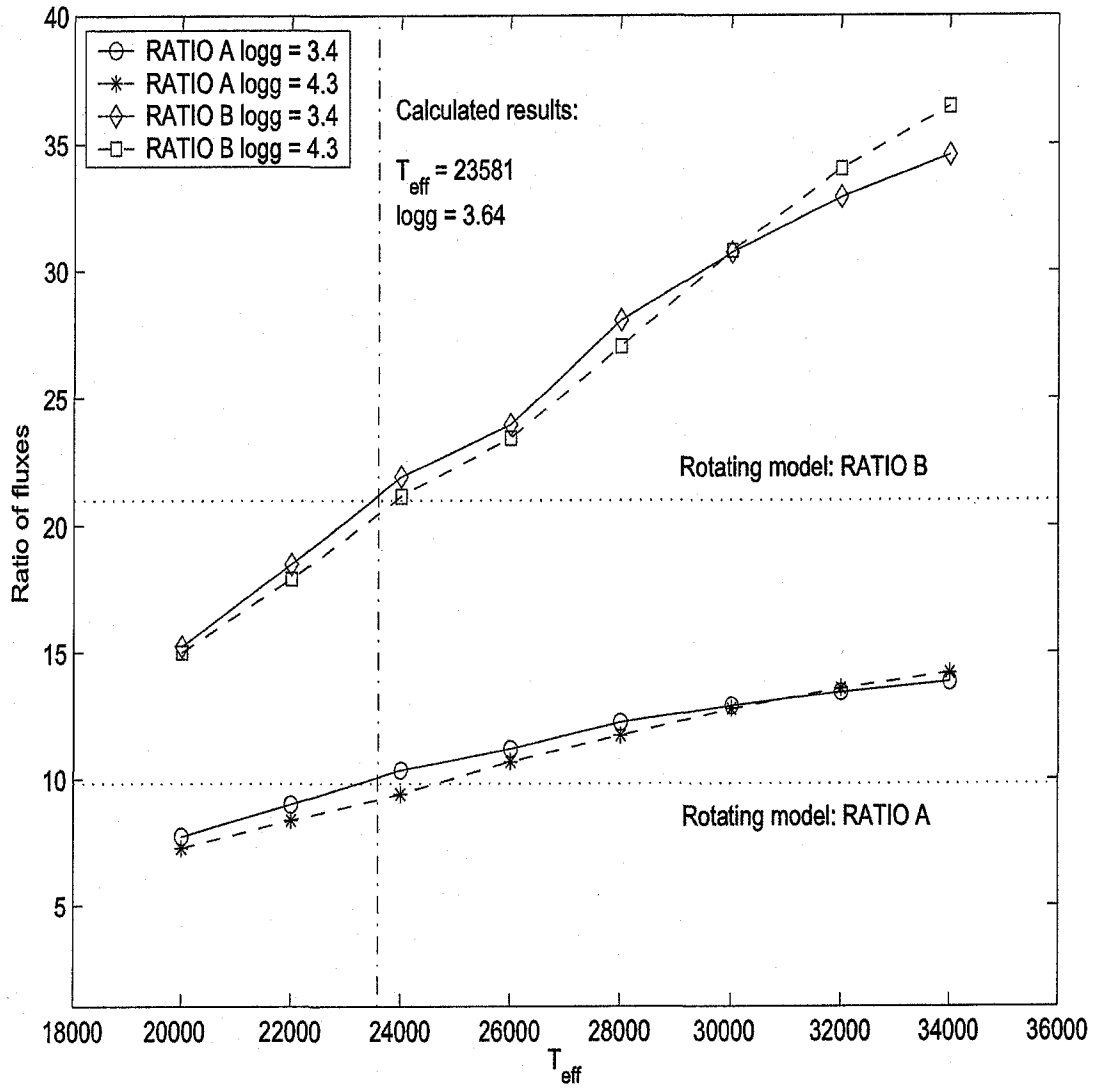


Figure 3.4: Flux ratios A and B as functions of temperature for both $\log g = 3.4$ and 4.3 . Horizontal dotted lines give the flux ratios for the model being determined. The vertical dot-dash line represents the final calculated T_{eff} and $\log g$ for the rotating SED.

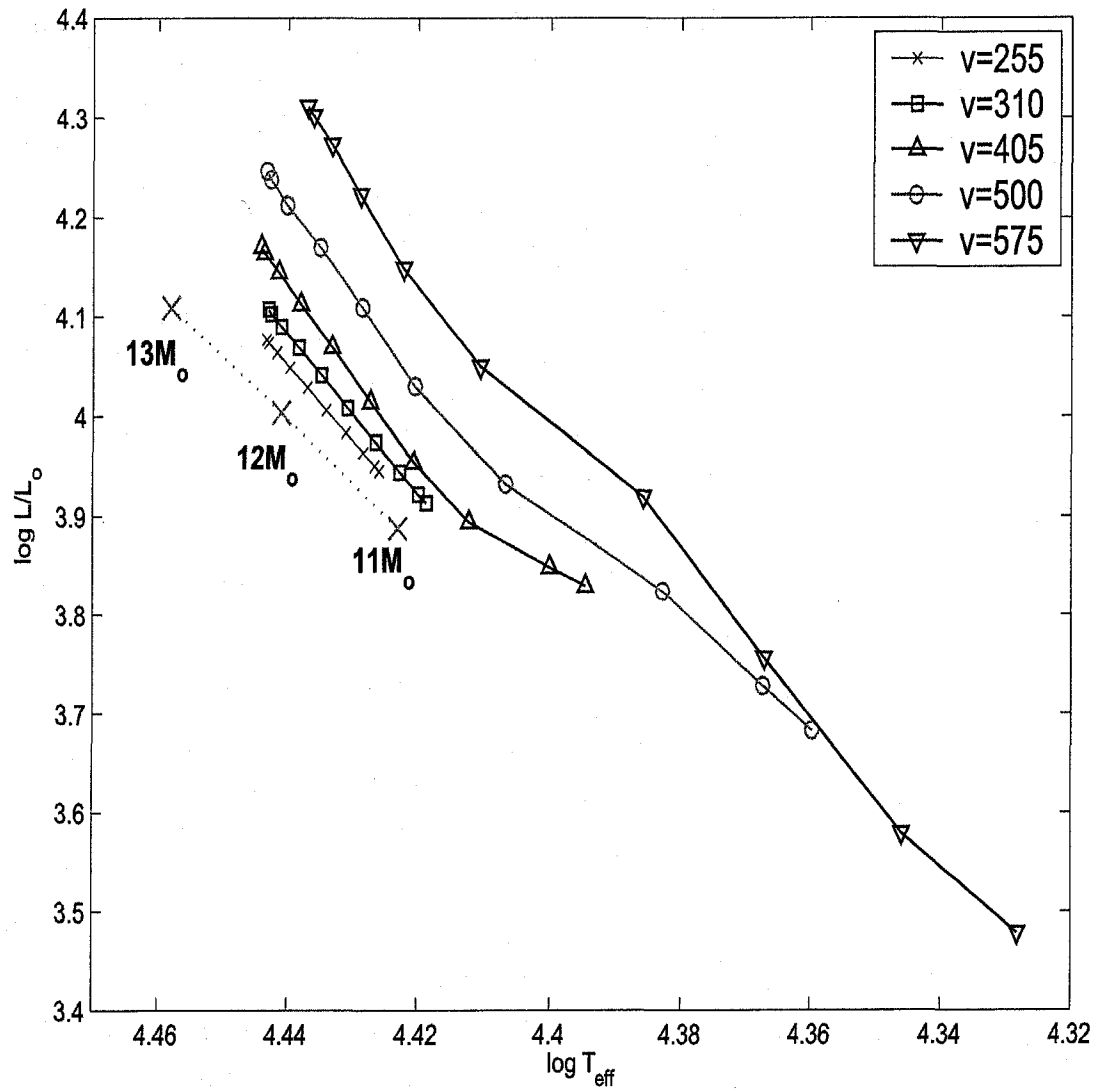


Figure 3.5: Inclination curves for uniformly rotating $12 M_{\odot}$ models at $v = 255\text{--}575 \text{ km s}^{-1}$. Note that critical rotation is approximately 600 km s^{-1} . ZAMS models at $11, 12, 13 M_{\odot}$ are given for scale, show that a uniform rotation rate of only 255 km s^{-1} can shift a star's apparent location by up to the equivalent of a solar mass.

known luminosity and temperature. It was found that the uncertainties in luminosity decreased as the luminosity increased, ranging from around 1% to 6%, whereas the uncertainties for temperature increased as the temperature increased, ranging from around 0.1% to 0.6%. The reason that the uncertainties in luminosity were an order of magnitude larger is likely because the luminosity was taken from the integral of the whole SED, which contained the PHOENIX uncertainties. The temperature, however, was found by comparing flux ratios calibrated against spectra containing the same uncertainties. Fig. 3.6 shows selected inclination curves, along with the uncertainties varying with temperature and gravity.

3.2.1 UNIFORM ROTATION

Fig. 3.7 shows inclination curves for 13 uniformly rotating models of $12 M_{\odot}$. Models were calculated for rotational velocities of 0, 50, 100, 150, 210, 255, 310, 350, 405, 450, 500, 550, and 575 km s^{-1} . Some non-rotating ZAMS models of various sizes are shown to lend a scale to the curves, and as can be seen, even rotation rates as low as 255 km s^{-1} can change a star's position on the HR diagram by the equivalent of an entire solar mass. The length of the 575 km s^{-1} curve is a shift of approximately 6 or $7 M_{\odot}$ along the ZAMS. At this velocity the luminosity changes from approximately $3000 L_{\odot}$ to $20500 L_{\odot}$, or by a factor of about 7. The change in T_{eff} is from approximately 21300 K to 27400 K, which corresponds to a range in spectral type from approximately B0.5 to B2 (Boehm-Vitense, 1981), or a change in U-B of approximately 0.14 (Cramer, 1984).

For small rotation velocities, the differences from one inclination to the next are small, resulting in a relatively straight line on the HR diagram. The straight line becomes curved as the rotation rate increases and the differences between points become larger.

Another feature of note is that the lines all appear parallel and quite close to the ZAMS. Rotation increases the component of centrifugal acceleration and lowers the effective gravity of the star, and hence the apparent mass. Therefore, to first order, a rotating star appears much like a non-rotating star of smaller mass, hence occupying a similar location near the ZAMS.

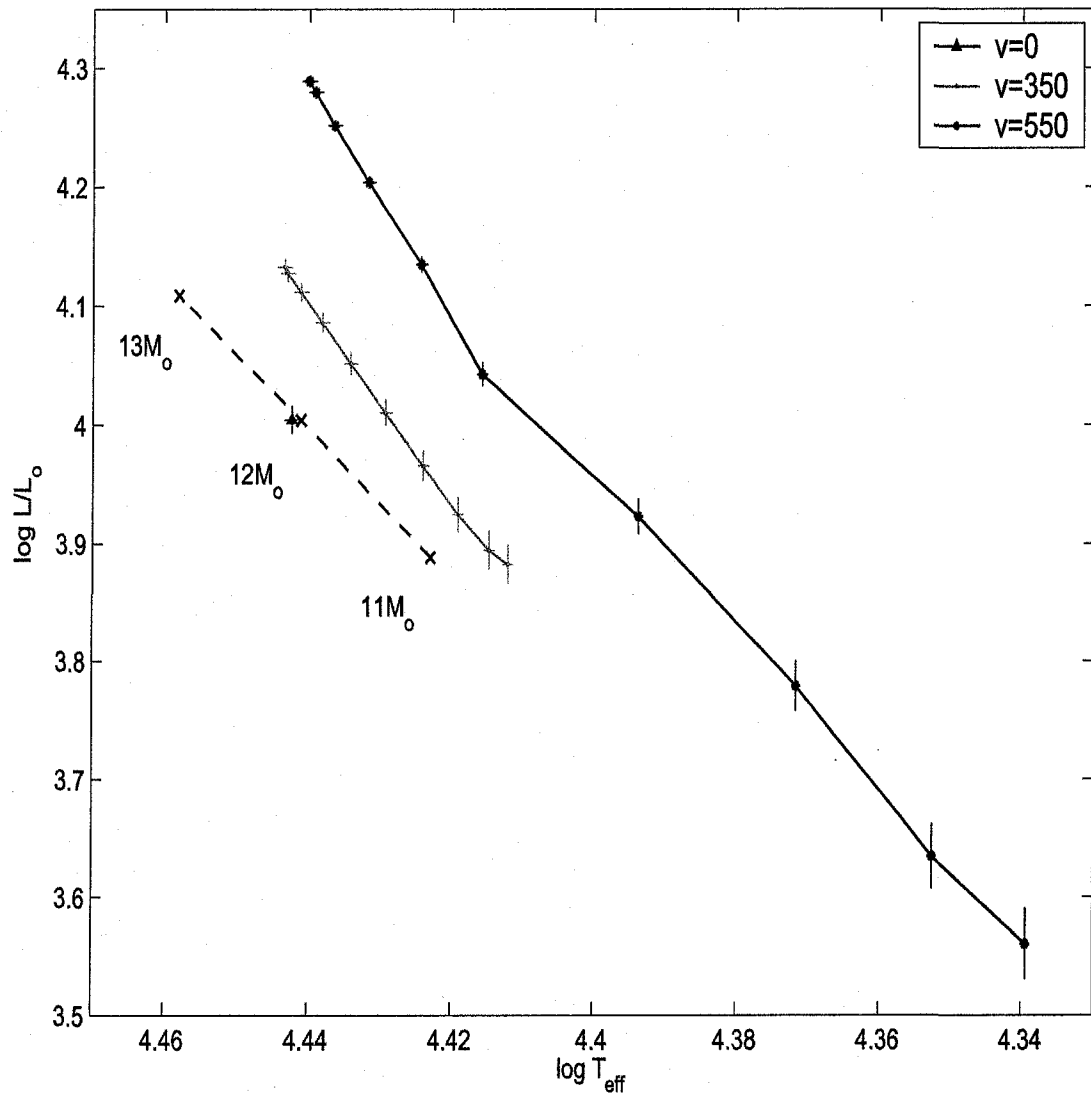


Figure 3.6: Selected inclination curves from Fig. 3.5 given with error bars. Uncertainties in luminosity increased with decreasing luminosity, while uncertainties in temperature increased with increasing temperature.

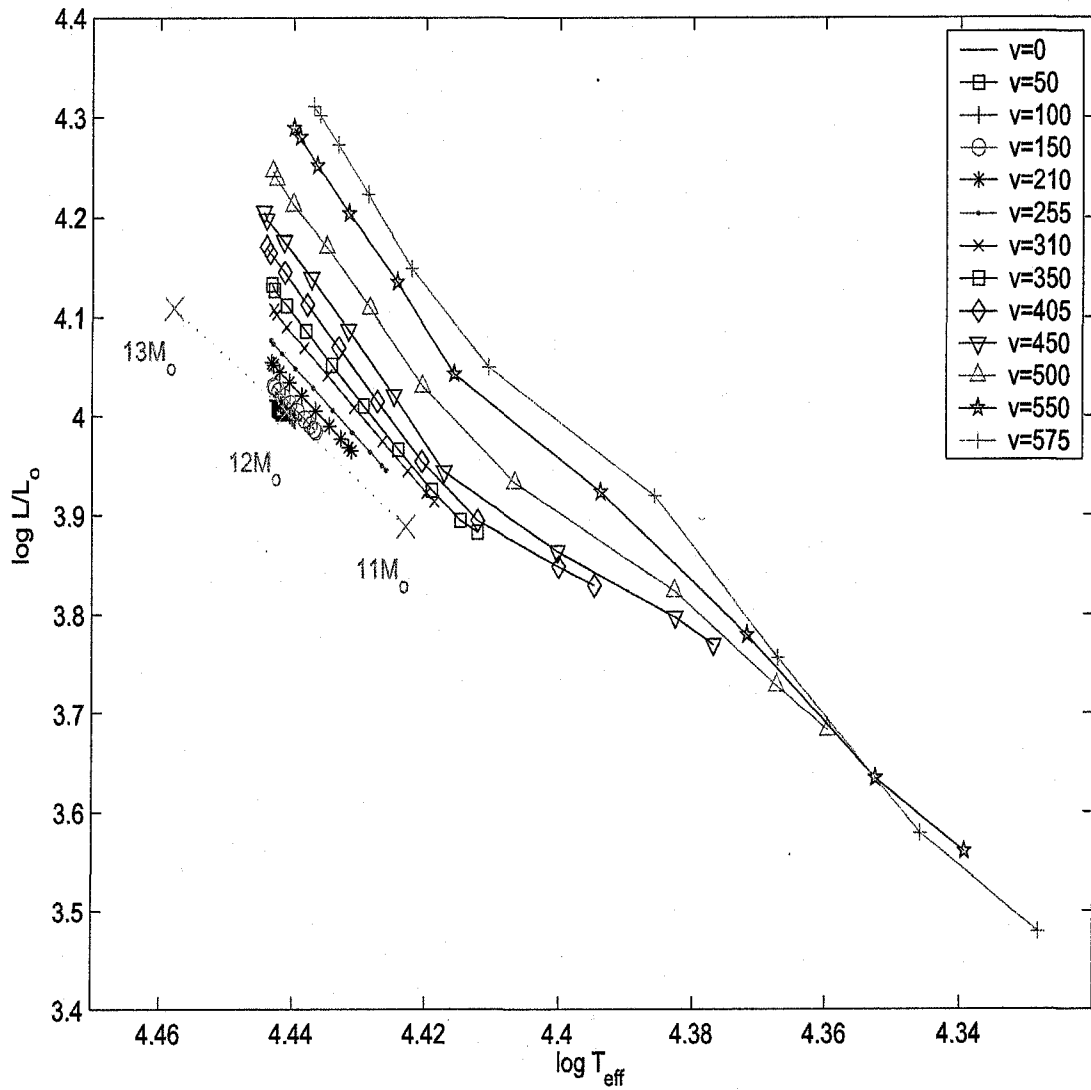


Figure 3.7: 13 inclination curves calculated for $12 M_{\odot}$ uniformly rotating stars from $v = 0$ to 575 km s^{-1} . As the distance between points increases, the curves become less linear. Note that the most significant changes are evident when the star is viewed nearly equator-on, where the star becomes much cooler.

The rotational velocity curves shown in Fig. 3.8 use the same models, but follow each inclination as the rotation rate increases. The most pronounced changes in the apparent location on the HR diagram are evident when viewed from the star's equator. As the star's rate of rotation increases, the equatorial radius also increases and the effective temperature there drops significantly. Because $F \propto T^4$, that in turn creates a significant drop in luminosity. Pole-on, the luminosity increases steadily with increasing rotation, as more and more of the flux is directed towards the poles by the increasingly oblate shape. Equator-on, one sees the most drastic changes, as that is where the temperature changes from the oblate shape are the most apparent.

3.2.2 DIFFERENTIAL ROTATION

While there has been evidence put forward to suggest that B stars are differentially rotating (Stoeckley, 1968), no solid conclusions have ever been reached. That differential rotation creates a bigger spread in luminosity than uniform rotation was a well known qualitative result that was confirmed by Collins & Smith (1985).

I will first compare three $10 M_{\odot}$ models rotating at 120 km s^{-1} with $\beta = 0, 1,$ and 2 (as defined in Eqn. 2.1). $\beta = 0$ signifies uniform rotation, while $\beta = 2$ is the maximum possible amount of stable differential rotation. Fig. 3.9 shows that differential rotation can have very interesting effects on the inclination curve. The variation in both luminosity and effective temperature with inclination, greatly increases with β , and the curve is no longer a straight line in the HR diagram, as it was for uniform rotation. A decreasing differential rotation law thus has the effect of making a star appear to be rotating much faster than it actually is if one assumed uniform rotation.

Fig. 3.10 shows three $10 M_{\odot}$ models rotating at 240 km s^{-1} with $\beta = 0, 0.6,$ and 1.2 . The same trends indicated by Fig. 3.9 are apparent, though to a lesser extent. While smaller changes in β will clearly produce smaller effects on the inclination curve, it can be stated that the inclination curve, and hence a rotating star's observed location on the HR diagram is very sensitive to the amount of differential rotation.

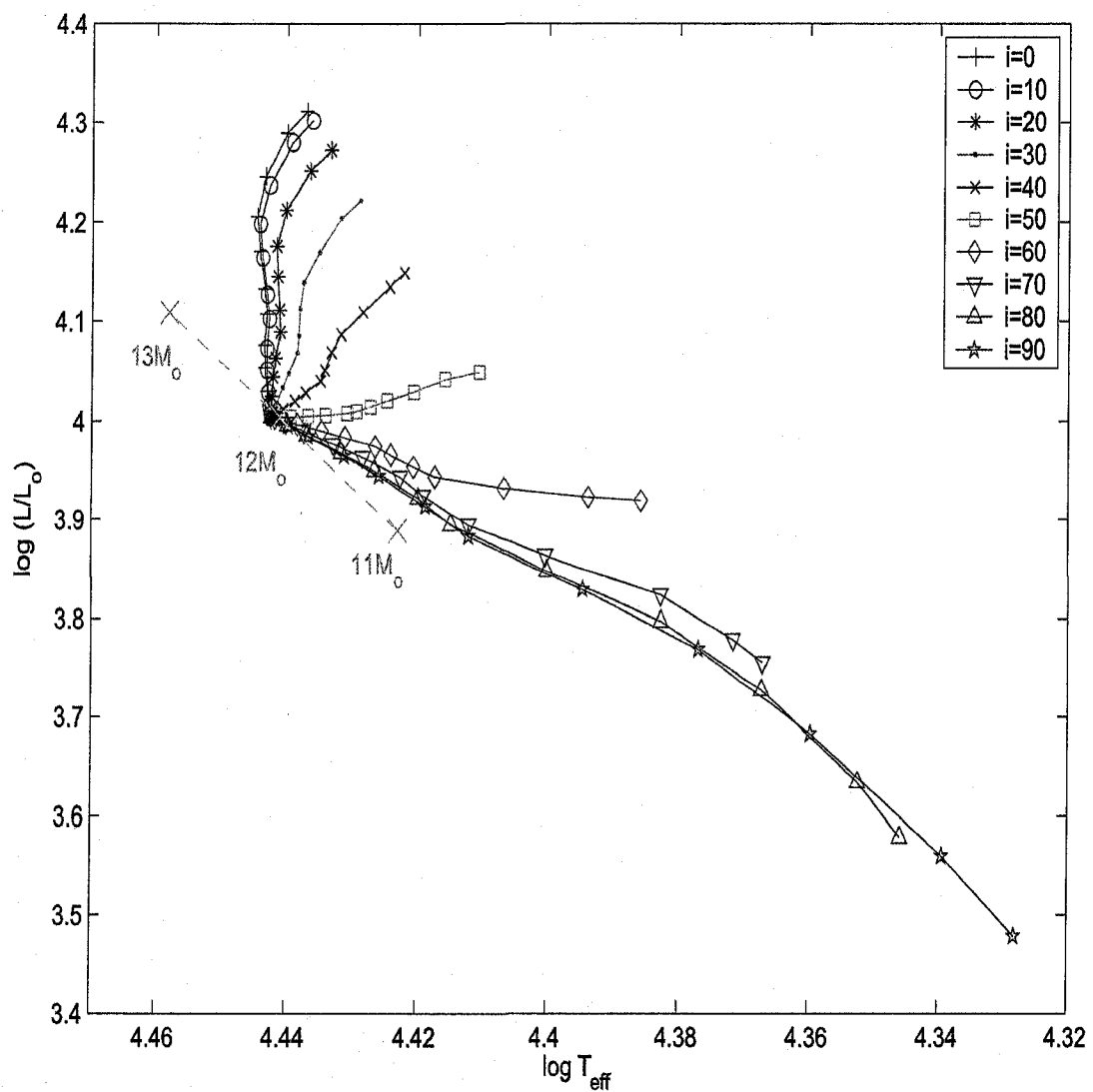


Figure 3.8: Rotational velocity curves showing each inclination as a function of velocity. Models are the same as for Fig. 3.7.

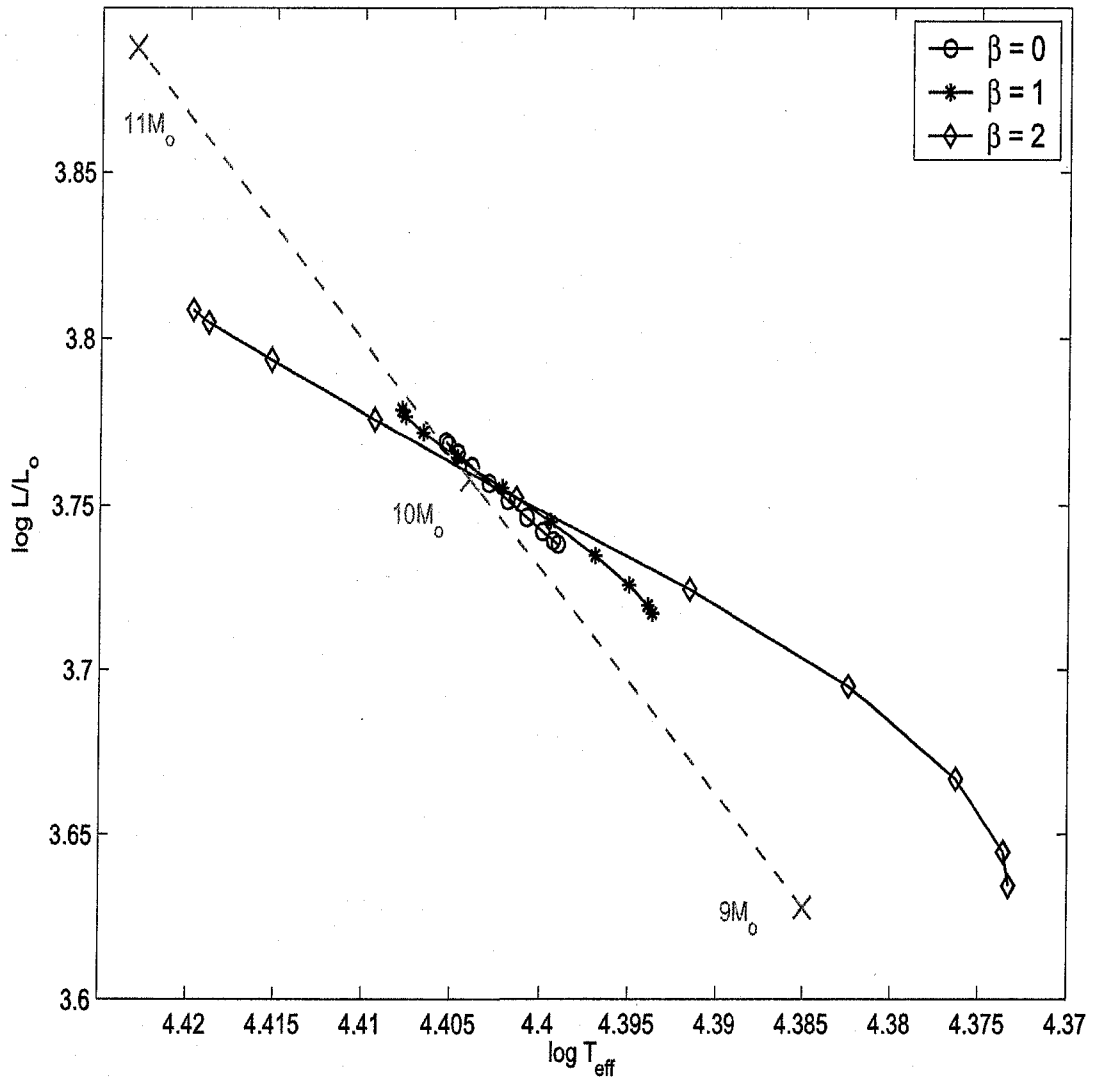


Figure 3.9: Inclination curves for $10 M_{\odot}$ models differentially rotating at $v = 120 \text{ km s}^{-1}$ with β increasing from 0 to 2. Non-rotating 9, 10, and $11 M_{\odot}$ models are shown for scale. Differential rotation makes the star appear to be rotating much more rapidly than it is if one assumed uniform rotation.

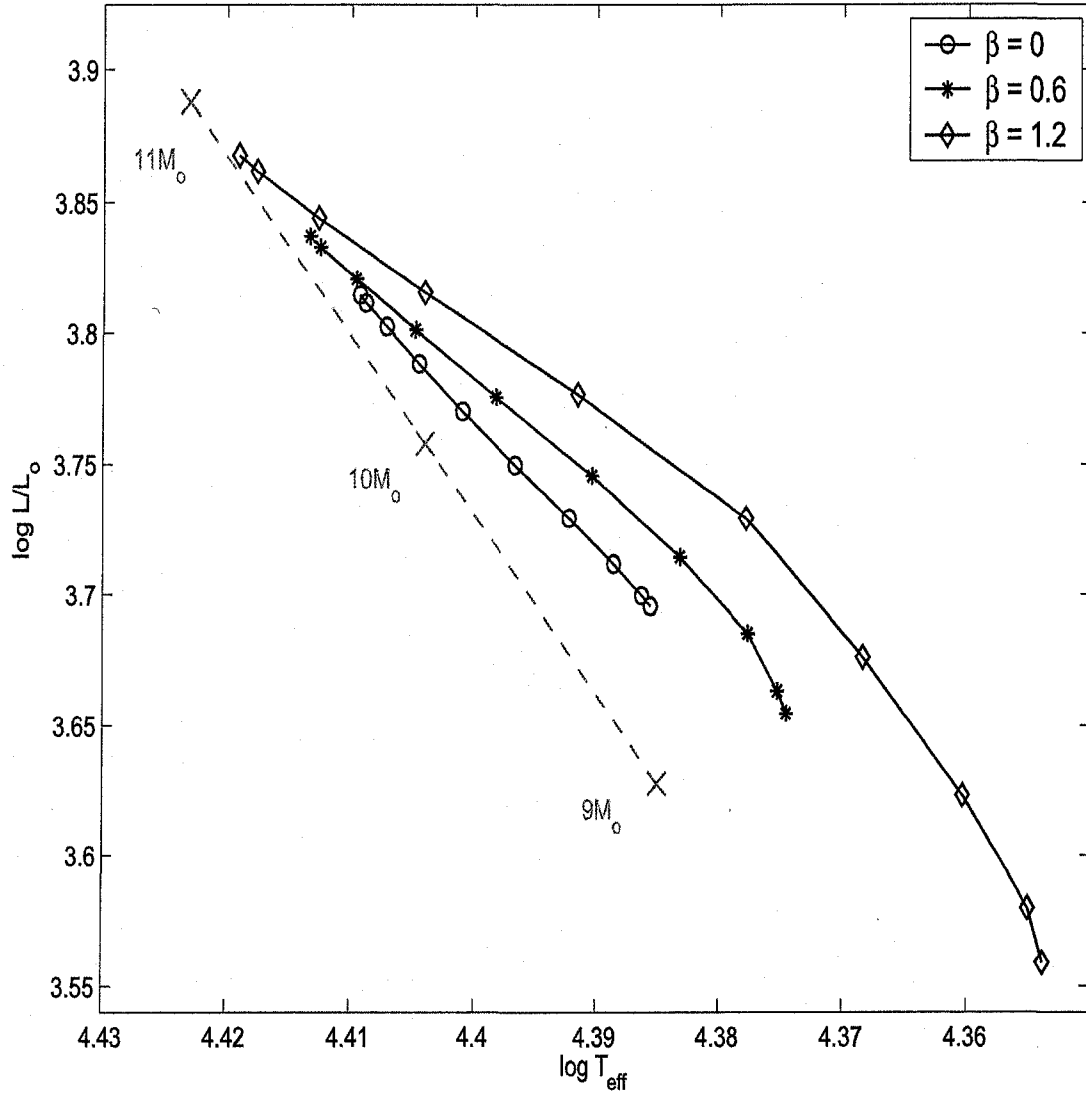


Figure 3.10: Inclination curves for $10 M_{\odot}$ models differentially rotating at $v = 240 \text{ km s}^{-1}$ with β increasing from 0 to 1.2. Non-rotating 9, 10, and $11 M_{\odot}$ models are shown for scale. Smaller differences in β have a smaller, but still distinctive effect on the inclination curve.

3.2.3 VON ZEIPPEL COMPARISON

Since von Zeipel's law is a frequently used approximation to 2D modelling, it is useful to determine its effects on the inclination curves. Lovekin *et al.* (2006) showed that von Zeipel's approximation breaks down as the rotational velocity gets large. The reason can be seen in Fig. 3.11, which compares the temperature profiles from the von Zeipel law to those from 2D calculations of ROTORC. In order to see how the differences affect the inclination curves, I followed the same procedure outlined in Section 3.2. The input for the integrator code was the same grid of non-LTE plane-parallel PHOENIX atmospheres. The only difference was that, instead of being shaped by a 2D ROTORC structure model, the spectrum of the rotating model was determined using a surface structure calculated from von Zeipel's theorem, i.e. $T_{eff} \propto g_{eff}^{1/4}$, and a Roche surface potential. The constant of proportionality was set by forcing the von Zeipel and ROTORC temperatures curves to match at a colatitude of 58° . The von Zeipel model temperatures go much lower at the equator at high rotation velocities because the von Zeipel law predicts T_{eff} goes to zero as the star approaches critical rotation.

The effect such differences have on the deduced SEDs can be seen in Fig. 3.12. The SEDs plotted there were again used to generate inclination curves using the method previously described. The final inclination curves are shown in Fig. 3.13. As expected from Fig. 3.11, the largest differences in the inclination curves between ROTORC and von Zeipel models occur for pole-on and equator-on orientations. The discrepancies between the two models are outside the uncertainties described above for any rotation velocity greater than about 350 km s^{-1} . Therefore, one should avoid using von Zeipel's law to calculate inclination curves for rapidly rotating stars.

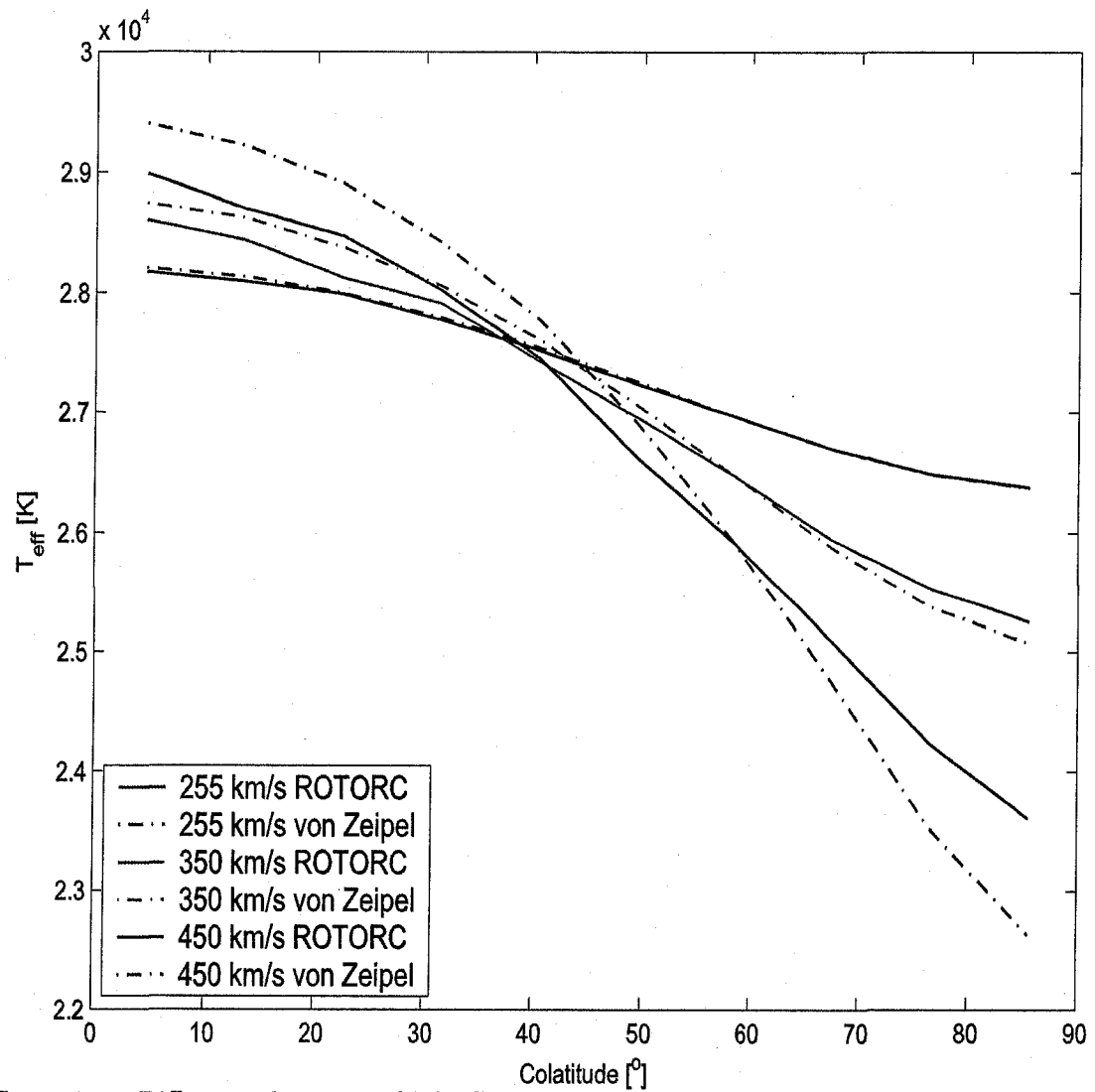


Figure 3.11: Differences between ROTORC and von Zeipel temperature profiles for $12 M_{\odot}$ models with increasing uniform rotation velocities. The differences become significant for rotational velocities above about 350 km s^{-1} .

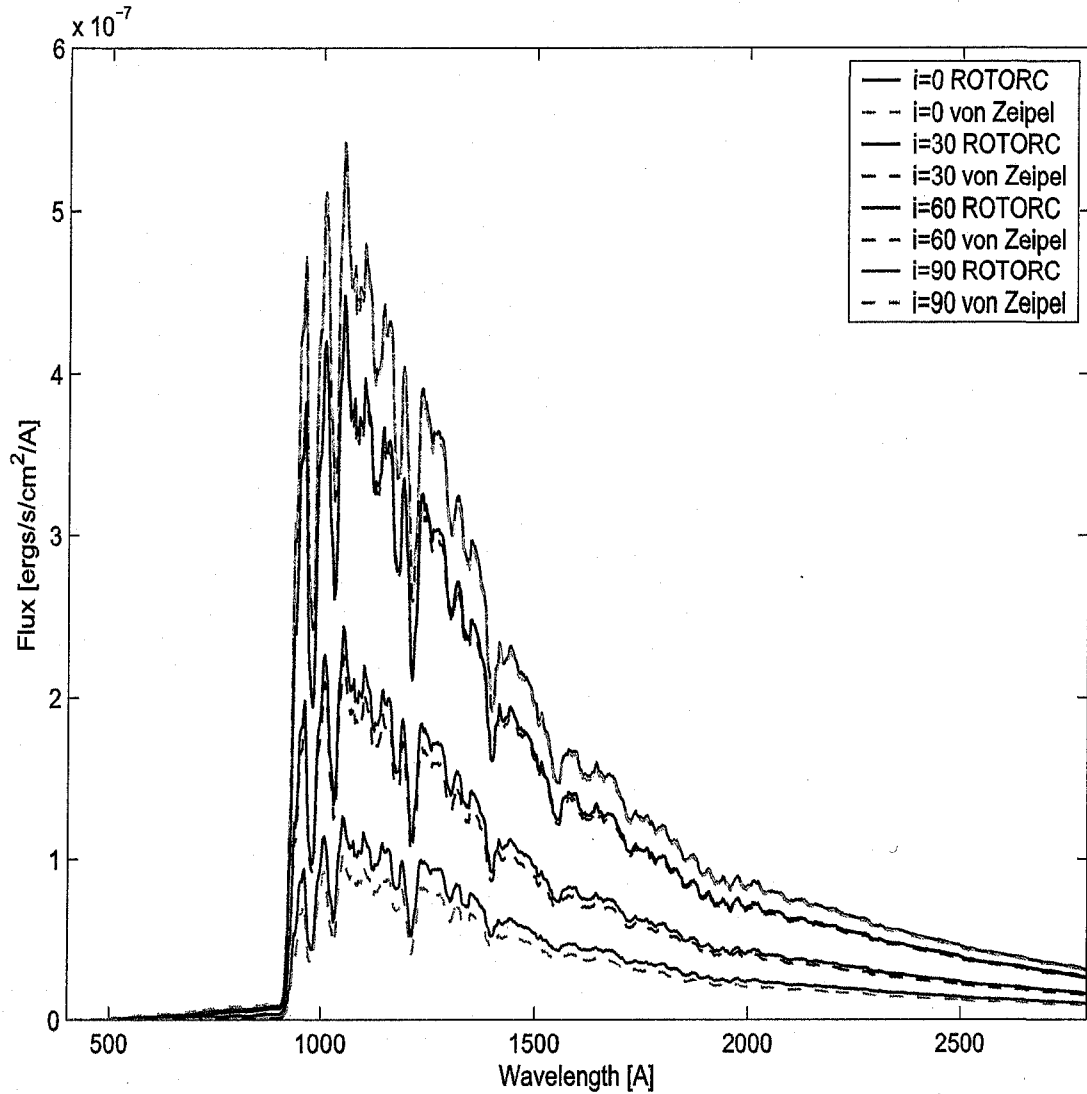


Figure 3.12: Differences between integrated ROTORC and von Zeipel model fluxes for $v = 500 \text{ km s}^{-1}$, for $12 M_{\odot}$ models at $i = 0, 30, 60,$ and 90° . Flux is given at Earth from a distance of 40 pc. As shown in the temperature differences of Fig. 3.11 the differences between ROTORC and von Zeipel model become more pronounced at the equator.

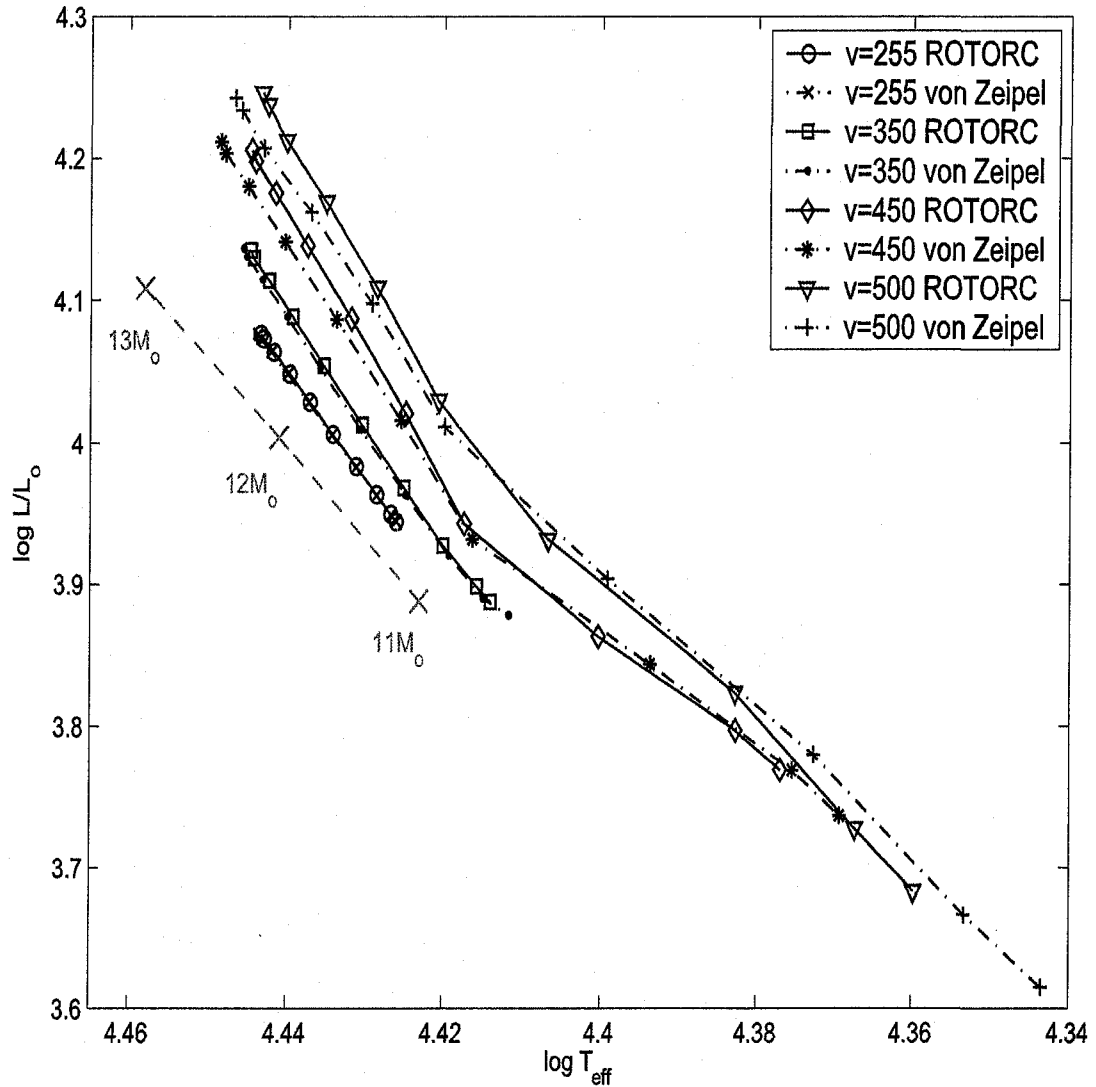


Figure 3.13: ROTORC vs. von Zeipel model inclination curves for $12 M_{\odot}$ uniformly rotating models. The differences between them exceed the uncertainties for any rotational velocity greater than around 350 km s^{-1} .

CHAPTER 4

LINE PROFILES

This section uses the line mode option in CLIC to synthesize individual spectral lines. The intensity spectra, $I_\lambda(\lambda)$, files created by PHOENIX were used by CLIC to generate rotationally broadened line profiles without the need for any mathematical approximations. Limb darkening is automatically incorporated by CLIC because it integrates over the surface of the star and takes the appropriate components of the intensity in the direction of the observer. It does it at every wavelength, eliminating the uncertainties arising from a wavelength dependent limb darkening law. Gravity darkening is accounted for by the shape of the structure model given by ROTORC. It therefore allows the direct calculation of the rotational broadening of a line profile.

This chapter first compares the effects of differential rotation on line profiles, and then compares lines calculated from a von Zeipel structure model with those from a ROTORC model.

4.1 EFFECTS OF DIFFERENTIAL ROTATION

Determining a star's rotation law is a challenge that has long faced stellar astrophysicists. While no rotation law can be determined definitively, there has been much effort to determine the effects that differential rotation might have on line profiles. I have discussed previously how increasing differential rotation tends to pinch in the wings of a spectral line and deepen its core. Previous studies (e.g. Stoeckley (1968); Reiners & Schmitt (2002)) have suggested, reasonably, that decreasing differential rotation does the exact opposite, flattening the core and broadening the wings. However, those studies featured primarily mathematical approximations for limb darkening and gravitational darkening, and focused more on increasing differential rotation, with only mild cases of decreasing differential rotation. This chapter not only improves on the method of calculation by using integrated

intensities, but also explores more extreme cases of decreasing differential rotation.

The spectral lines calculated use the same set of differentially rotating structure models that were used to generate the inclination curves in the previous chapter. Two different surface equatorial rotation velocities were considered, and three different rotation profiles were compared for each. The quantity of most interest is the surface rotation velocity as a function of colatitude shown in Fig. 4.1 for the $10 M_{\odot}$, $v=120 \text{ km s}^{-1}$ case. Note that for very high values of β the largest surface rotational velocity need not be at the equator.

There are slight differences in temperature between the models, as well as differences at each rotation rate, which make the continuum flux slightly different. All the lines were therefore shifted to have the same continuum value so that the effects of the rotational broadening alone could be considered. The amount of shifting was generally quite small.

Fig. 4.2 shows the relatively weak C II $\lambda 4268$ line for the star viewed equator on, rotating at 120 km s^{-1} with differential rotation parameters of $\beta = 0, 1, \text{ and } 2$. Also shown in Fig. 4.2 is the C II $\lambda 4268$ line broadened for a uniformly rotating star at 150 and 180 km s^{-1} . It can be seen that differential rotation broadens the wings of the line and flattens and brightens the core. No amount of uniform rotation will create a line profile that fits the differentially rotating ones. That is the expected behaviour of a line broadened by decreasing differential rotation, and represents the type of result typically seen in the past. The differences seen in Fig. 4.2, while distinct, are not so strong as to be easily detected. The principal reason is that previous studies were not concerned with more extreme decreasing differential rotation, and the cases they did study focused mainly on equator-on views. Many researchers detailed in the introduction found that the subtle effects of differential rotation on line profiles only became significant when observed in the Fourier domain.

Here the advantages of the present research become clear, for with the combination of ROTORC, PHOENIX, and CLIC, it is possible to create a detailed view of a line from any inclination angle, broadened by nearly any rotation law. I will show, observing a line from a strongly differentially rotating star from higher inclination angles can reveal distinct features of the line profile that do

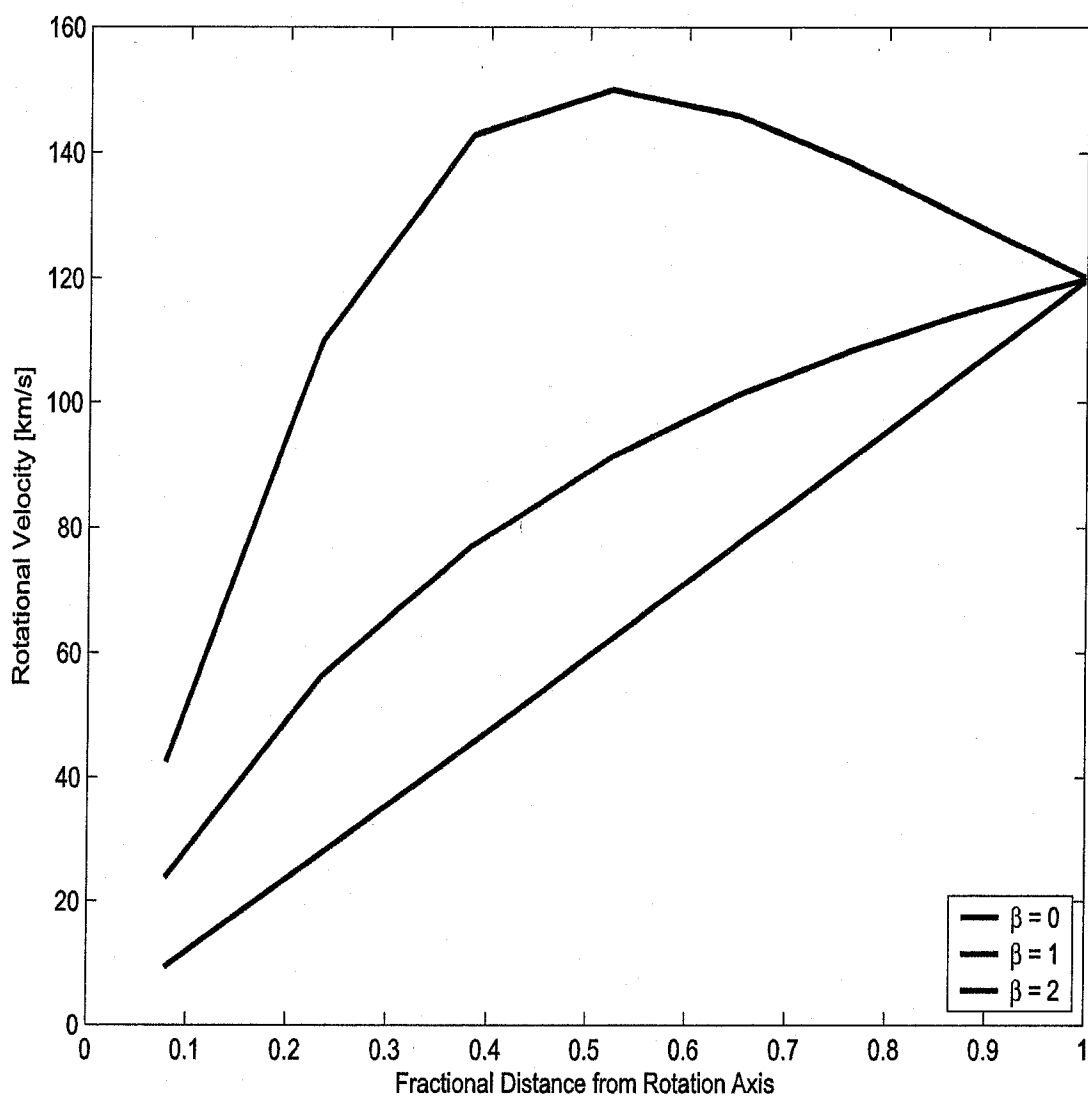


Figure 4.1: Surface rotation velocity as a function of colatitude for various rotation profiles. All models are $10 M_{\odot}$ and have surface rotational velocities of 120 km s^{-1} . The most significant differences in rotation profiles occur between colatitudes of 10° and 60° .

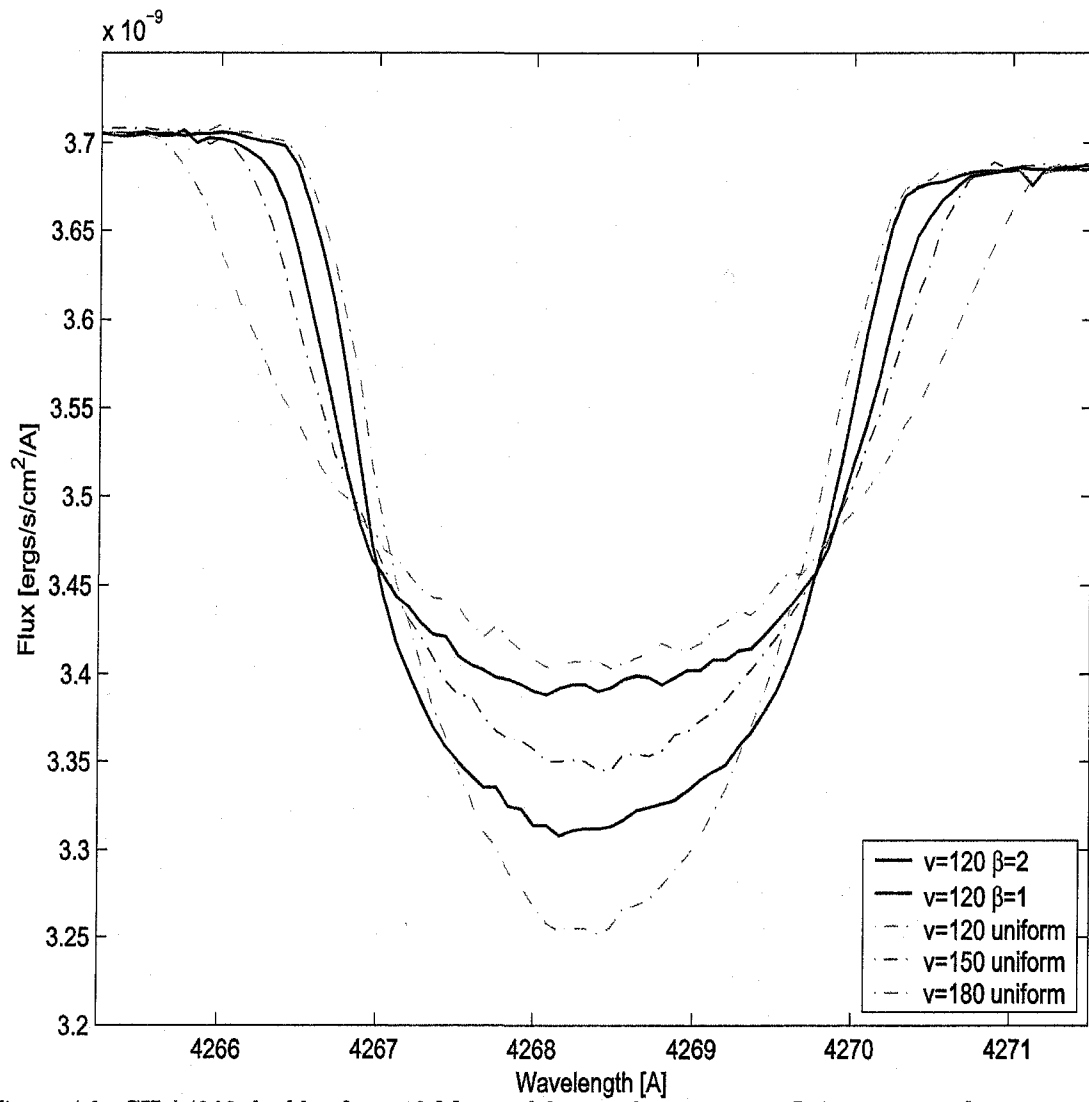


Figure 4.2: CII $\lambda 4268$ doublet for a $10 M_{\odot}$ model viewed equator on. It is a commonly seen view demonstrating the effects of differential rotation on line profiles.

not require a Fourier treatment. As can be seen in Fig. 4.1, the key differences between the rotation laws occur at the lower colatitudes, from about 10° to 60° .

C II $\lambda 4268$ is a doublet, therefore the remainder of the analysis focuses on the single line He I $\lambda 4923$ to show the effects arising from rotation alone.

Figs. 4.3 through 4.6 show how the He I $\lambda 4923$ line appears when unbroadened, and then at each inclination angle for $v=120 \text{ km s}^{-1}$ with the rotation profiles given in Fig. 4.1. Fig. 4.3 shows the unbroadened He I $\lambda 4923$ with the neighbouring O II $\lambda 4926$ line. Because the two lines are close together, they become blended as the star rotates. That accounts for the asymmetries in the lines shown in Figs. 4.4 through 4.6. It can be seen in Fig. 4.6 that lines viewed equator-on show the expected trends, however the more interesting features become apparent as the view becomes more pole-on. The lines for $\beta = 2$, and, to a lesser degree for $\beta = 1$, viewed from 10° to about 40° all show a central reversal, with the deepest parts of the lines migrating towards the wings. The shape is caused by the sections of the star closer to the rotation axis rotating faster than the parts at the equator. The parts of the star that produce the absorption in the core of the line are rotating faster than they would be under a uniform rotation law, and thus are absorbing further into the wings. This decreases the core absorption and increases the wing absorption sufficiently to produce a central reversal.

In probing the effects of differential rotation, I considered lines from different parts of the spectrum. It was found that stronger lines were not very sensitive to small changes in the surface structure of the models. Fig. 4.7 illustrates the effect for three inclination angles (30° , 60° , and 90°) for the H δ line from the same $10 M_\odot$, $V=120 \text{ km s}^{-1}$ models shown above. The same trends are present, but to such a modest degree that no decisive conclusions could be extracted from them. It was found that all Balmer series lines and most lines in the UV were too strong, and displayed very little sensitivity to differential rotation. However, many other weaker lines in the visual displayed the same trends as He I $\lambda 4923$. The differences in the Doppler width of the line profiles demonstrated in Figs. 4.4 through 4.6 are at most 0.5 \AA . Such a shift is quite prominent for weaker lines, but is not

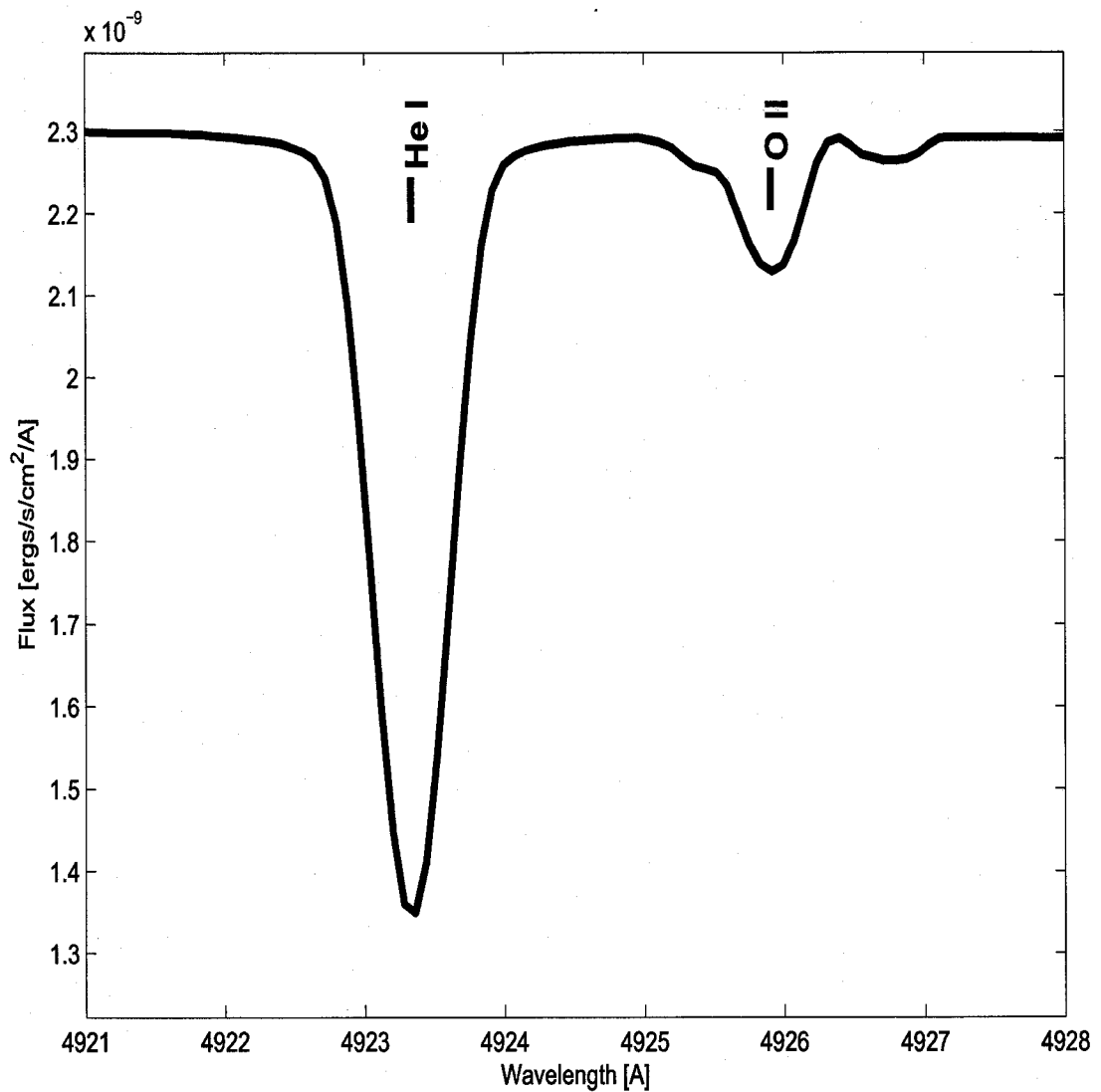


Figure 4.3: He I $\lambda 4923$ and O II $\lambda 4926$ for $10 M_{\odot}$ non-rotating model.

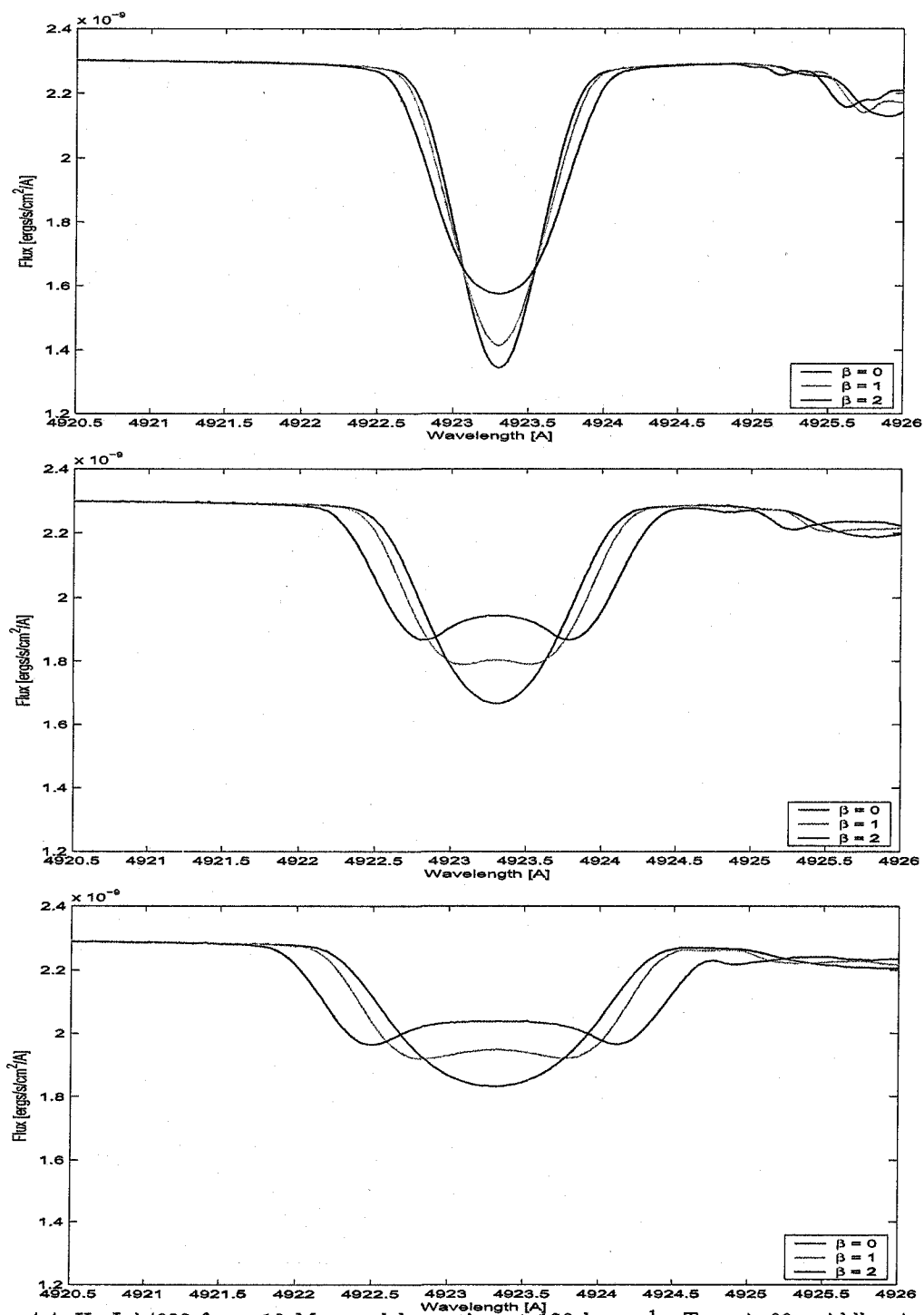


Figure 4.4: He I $\lambda 4923$ for a $10 M_{\odot}$ model rotating at 120 km s^{-1} . Top: $i=0^{\circ}$, middle: $i=10^{\circ}$, bottom: $i=20^{\circ}$. Note that the wavelength scale is constant but the flux scale varies from Figs. 4.4 to 4.6.

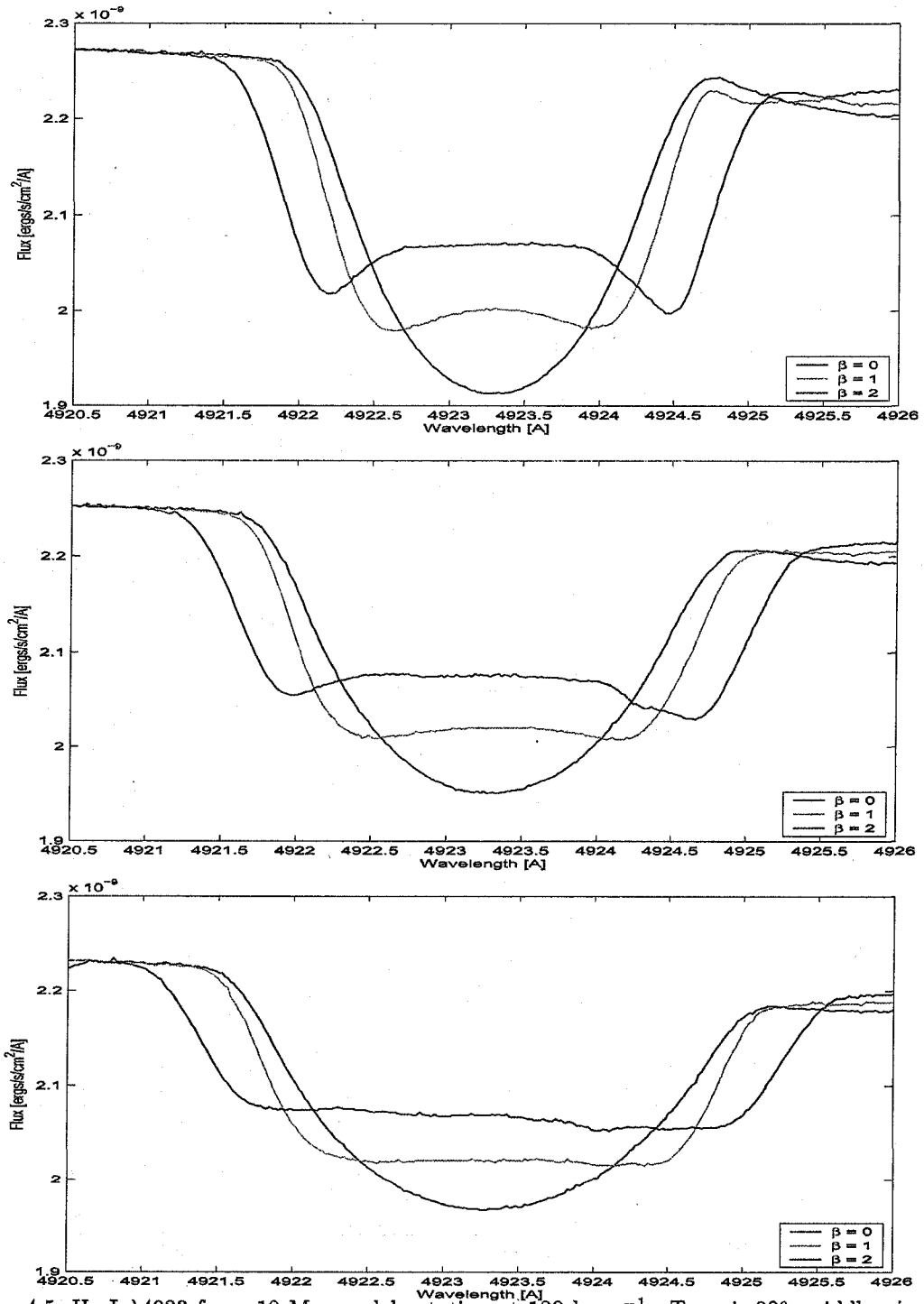


Figure 4.5: He I $\lambda 4923$ for a $10 M_{\odot}$ model rotating at 120 km s^{-1} . Top: $i = 30^\circ$, middle: $i = 40^\circ$, bottom: $i = 50^\circ$.

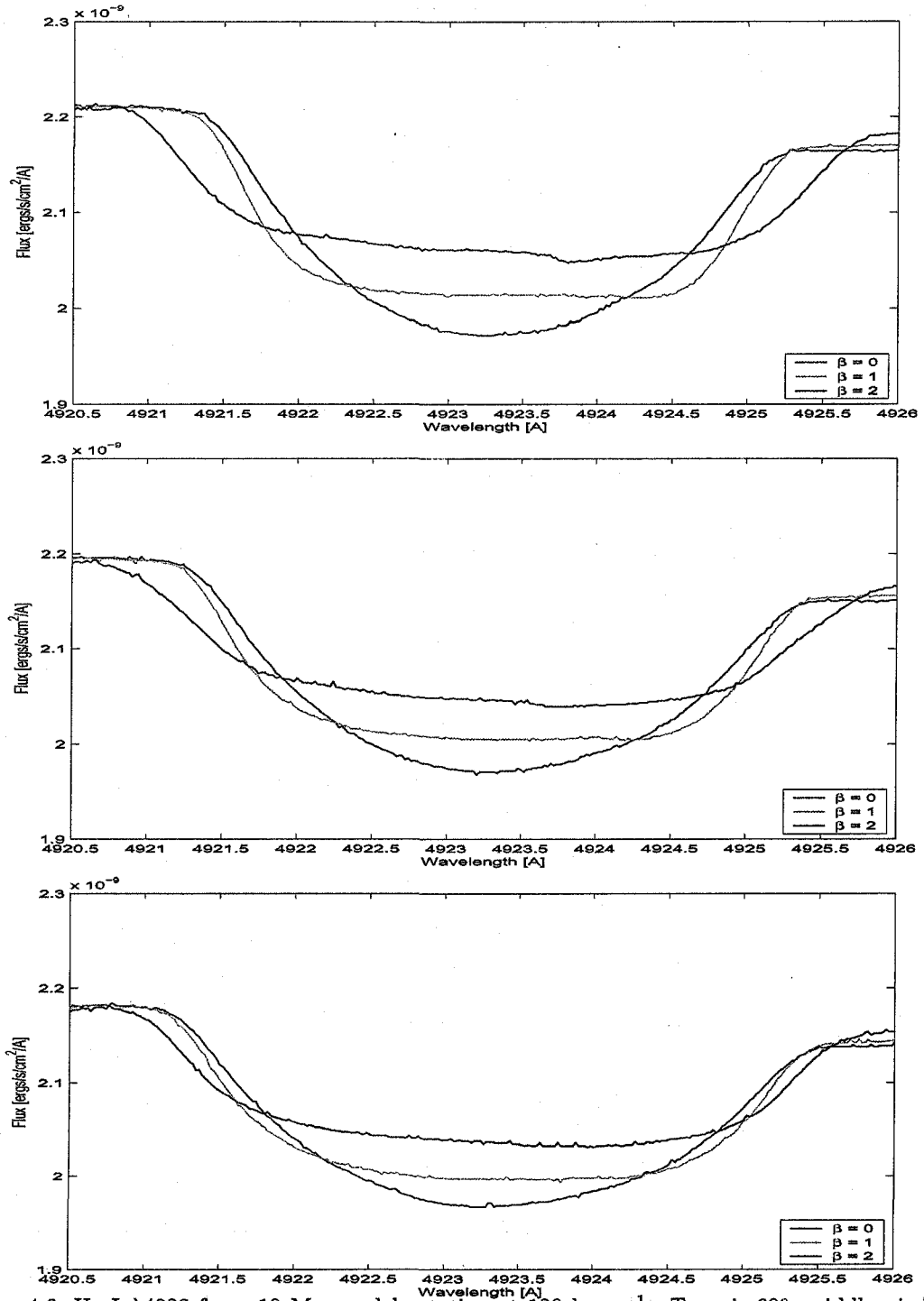


Figure 4.6: He I $\lambda 4923$ for a $10 M_{\odot}$ model rotating at 120 km s^{-1} . Top: $i=60^\circ$, middle: $i=70^\circ$, bottom: $i=90^\circ$.

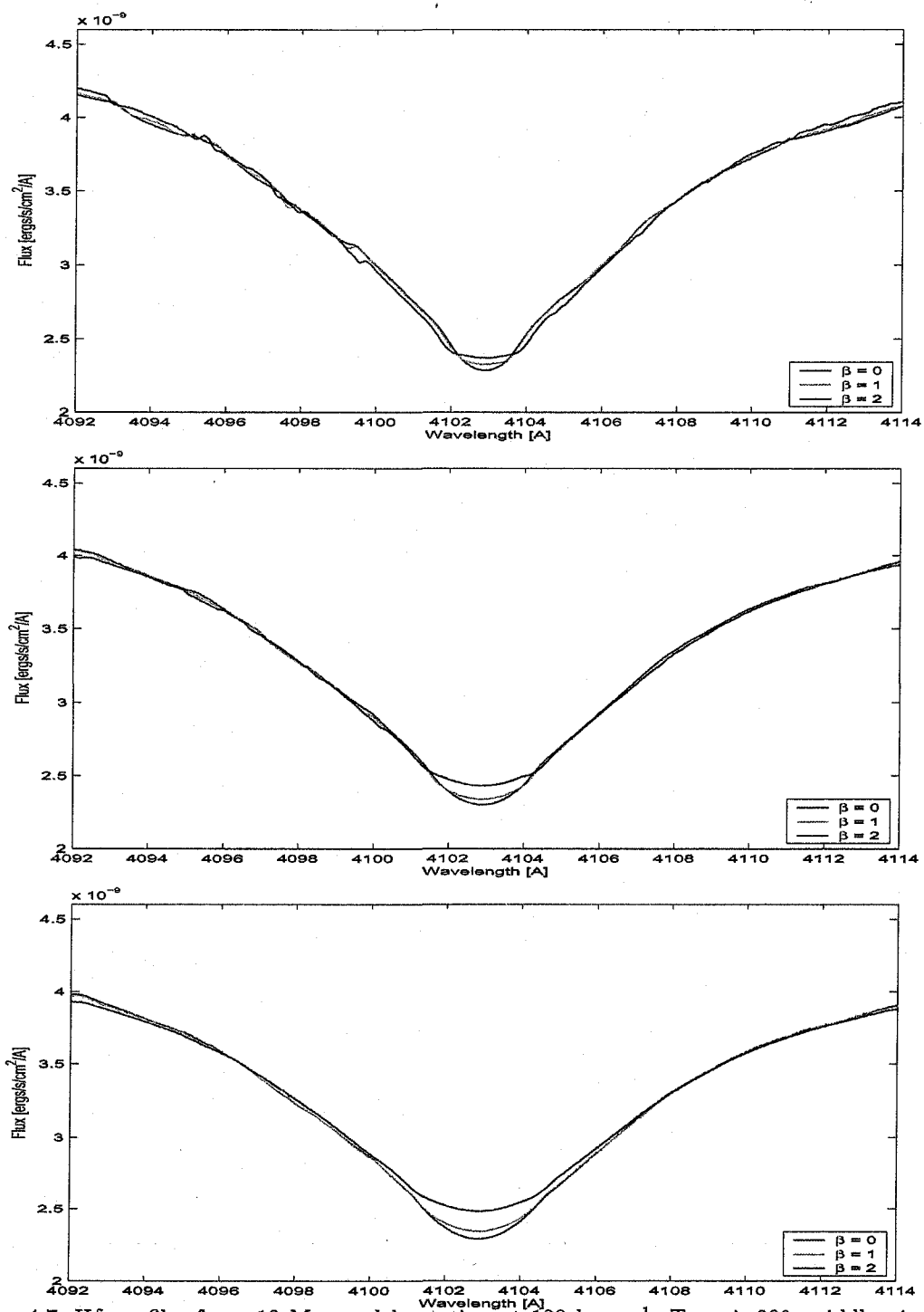


Figure 4.7: H δ profiles for a $10 M_{\odot}$ model rotating at 120 km s^{-1} , Top: $i=30^\circ$, middle: $i=60^\circ$, bottom: $i=90^\circ$.

for lines like H δ that are 10 to 20 Å wide. Furthermore, lines like H δ are considerably broadened by other mechanisms such as pressure broadening, which dominate the effects of rotation.

Figs. 4.8 and 4.9 show He I $\lambda 4923$ and H δ line profiles respectively, for 10 M_{\odot} models, rotating at $v=240 \text{ km s}^{-1}$ with $\beta = 0, 0.6, \text{ and } 1.2$. In Fig. 4.8 the trends seen at 120 km s^{-1} are still present. However, the line has now been broadened and flattened significantly. For any rotation velocities above $\sim 350 \text{ km s}^{-1}$ the line will be almost unrecognizable. The H δ line shown in Fig. 4.9, again shows the same trends but to a nearly insignificant degree.

While the results offer many new and unique ideas, it is necessary to analyze their limitations in order to put them into perspective. One limitation is the rotation velocity itself, as there is a distinct range of V_{rot} within which the diagnostic studied here is useful. If the star rotates slowly, then the rotational broadening will be negligible for any rotation law, and if it rotates too quickly, then the lines for which the traces of differential rotation are discernable will be blended into obscurity.

The next limitation is that the differences seen in the line profiles of the differentially rotating models may be too subtle to be practically observed. The differences in the Doppler widths of the line profiles arising from the effects of differential rotation range from about 0.1 Å to 0.5 Å. A spectrograph resolution of about $R = 10000 - 50000$ is therefore required. Stars brighter than an apparent visual magnitude of 14 observed with the ESPaDOnS spectrograph on the Canada-France-Hawaii Telescope can obtain a resolution of approximately $R = 70000$ for a one hour exposure (Donati, 2003). Therefore, a reasonable resolution within the abilities of present day optical telescopes could detect the effects predicted here.

I also investigate how distinguishable different values of β are. Figs. 4.4 through 4.6 show line profiles for β values of 0, 1, and 2. Because $\beta=2$ represents an extreme case of differential rotation, it is useful to examine further the range from $\beta = 0$ to 1. Fig. 4.10 shows the line profiles for a 10 M_{\odot} model rotating at 120 km s^{-1} for values of $\beta = 0, 0.2, 0.4, 0.6, 0.8, \text{ and } 1$. Uniform changes in β produce relatively uniform changes in the line profile. While it is difficult to determine a precise value of β at which differential rotation is clearly present, the broadening of the wings becomes significant

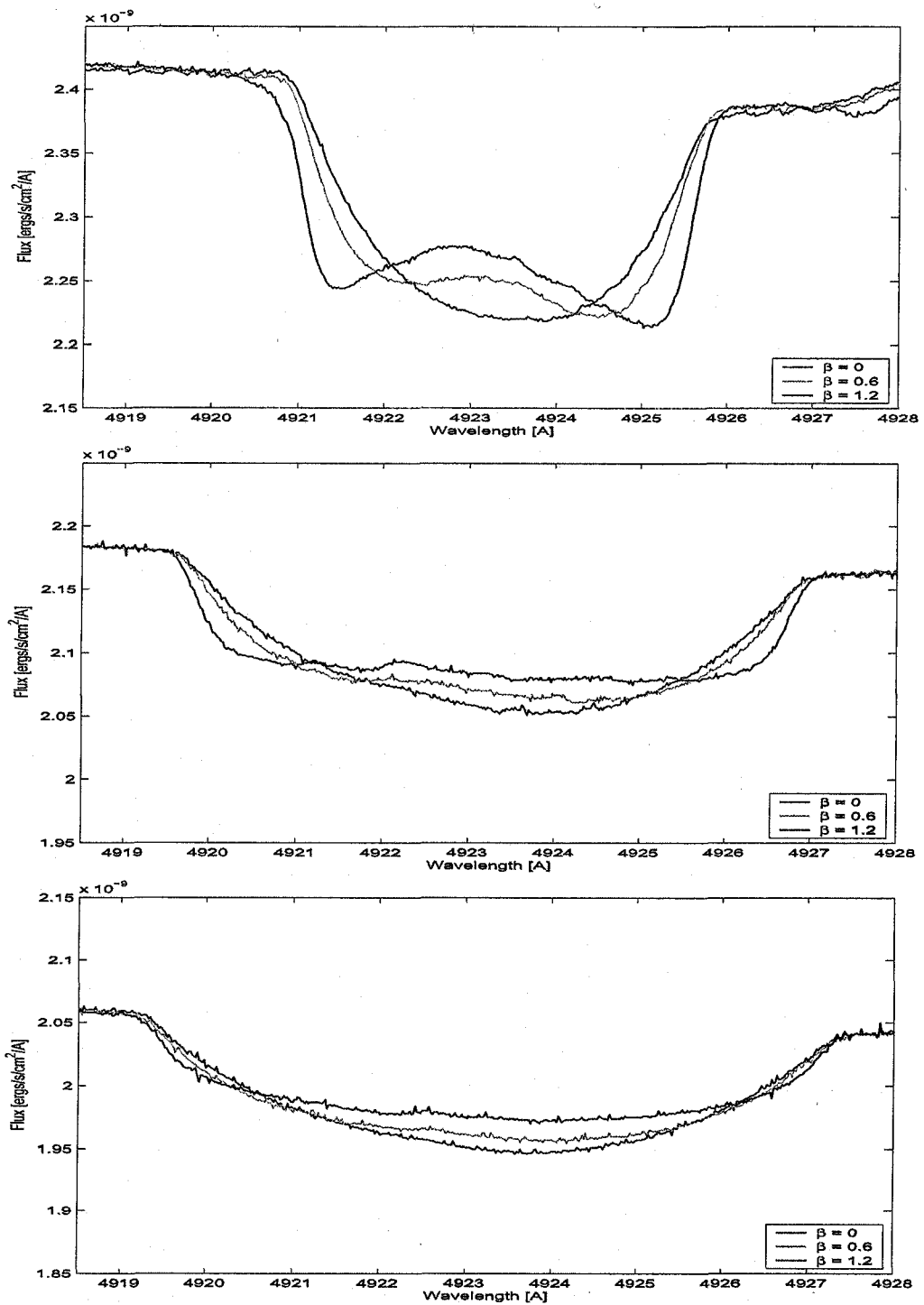


Figure 4.8: He I $\lambda 4923$ profiles for a $10 M_{\odot}$ rotating at 240 km s^{-1} Top: $i=30^\circ$, middle: $i=60^\circ$, bottom: $i=90^\circ$.

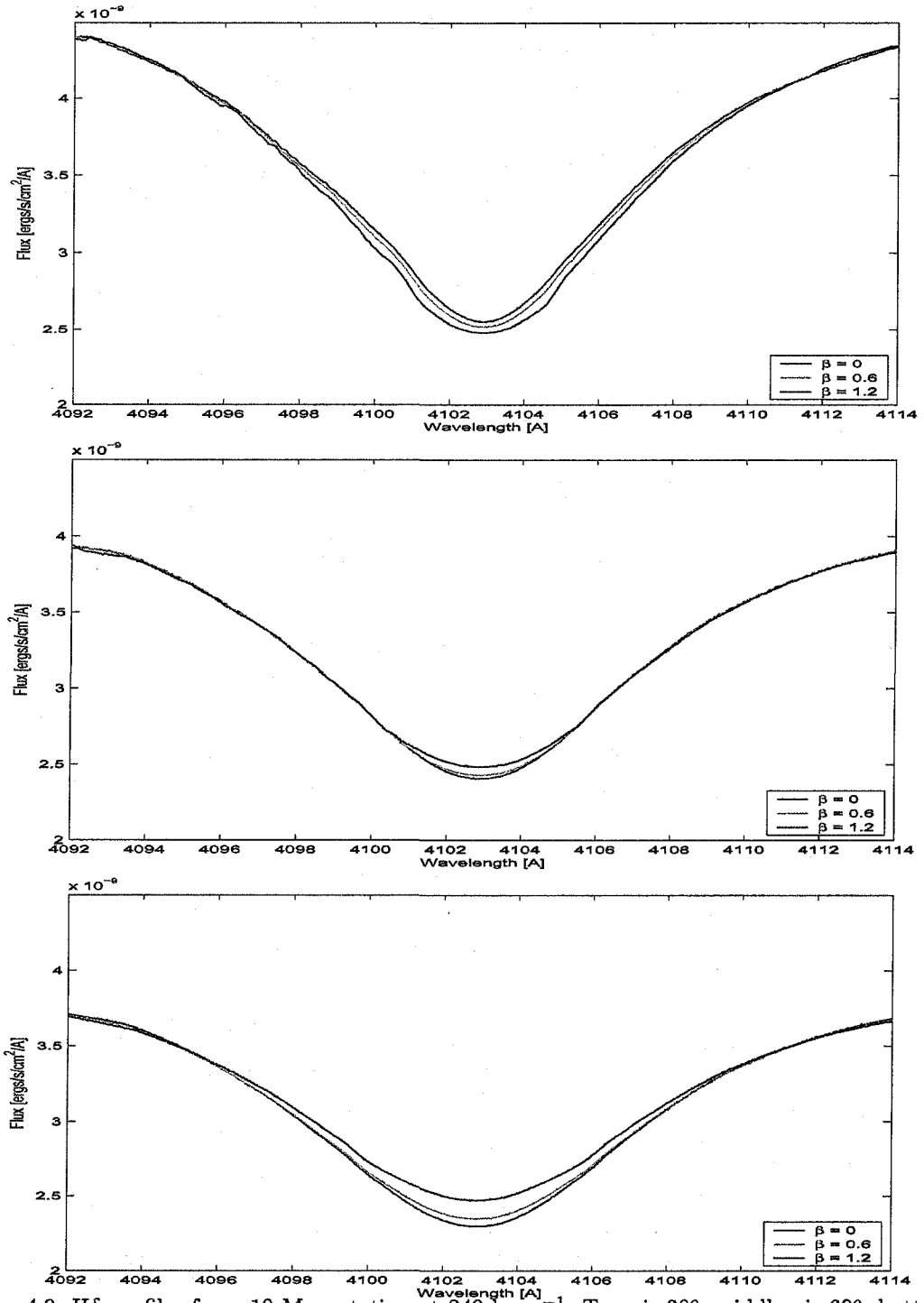


Figure 4.9: H δ profiles for a $10 M_{\odot}$ rotating at 240 km s^{-1} , Top: $i=30^\circ$, middle: $i=60^\circ$, bottom: $i=90^\circ$.

somewhere between $\beta = 0.4$ and 0.6 . That is a very realistic amount of differential rotation, which suggests that with further refinement, the method has the potential to be a powerful diagnostic for rotating stars.

A careful distinction must also be made at this point. A significant difference between the line profiles shown in Fig. 4.3 and Figs. 4.4 through 4.6 is the inclusion of Doppler broadening. In particular, the central reversals in the line profiles presented therefore arise from rotation alone. While that is certainly true for the work shown here, it does not necessarily follow that the observation of such features in a real star must be attributed to Doppler broadening. The preferential broadening in the core of the line, and even the central reversal could theoretically originate in another mechanism such as Zeeman splitting. This comment is put forward only as a caution, the investigation of which is beyond the scope of this work.

It is also of note that the lines become less smooth as the rotation rate increases. That can be attributed entirely to the quantized nature of the calculation. The sampling of our synthetic spectrum is 0.02 \AA , the same as the noise in the highly broadened lines (e.g. Fig. 4.8). A comparison of the highly broadened lines of Fig. 4.8 with the unblended lines of Fig. 4.3 confirms that the coarseness is a product of the rotation calculation, and not inherent to the line itself.

4.2 VON ZEIPEL'S LAW

Compared here are spectral lines calculated using the 2D ROTORC structure models with those calculated using von Zeipel's law. All models shown in this section are for a $12 M_{\odot}$ star and are uniformly rotating. The only differences in the calculation are the $\log g$ and T_{eff} as functions of colatitude between von Zeipel's law and ROTORC. Because the differences between von Zeipel's law and ROTORC are most apparent at the equator, only the $i = 90^{\circ}$ views are shown.

Fig. 4.11 shows He I $\lambda 4923$ at five different rotational velocities: 50, 100, 210, 350, and 500 km s^{-1} . The differences between von Zeipel's law and ROTORC are so negligible that the solid and

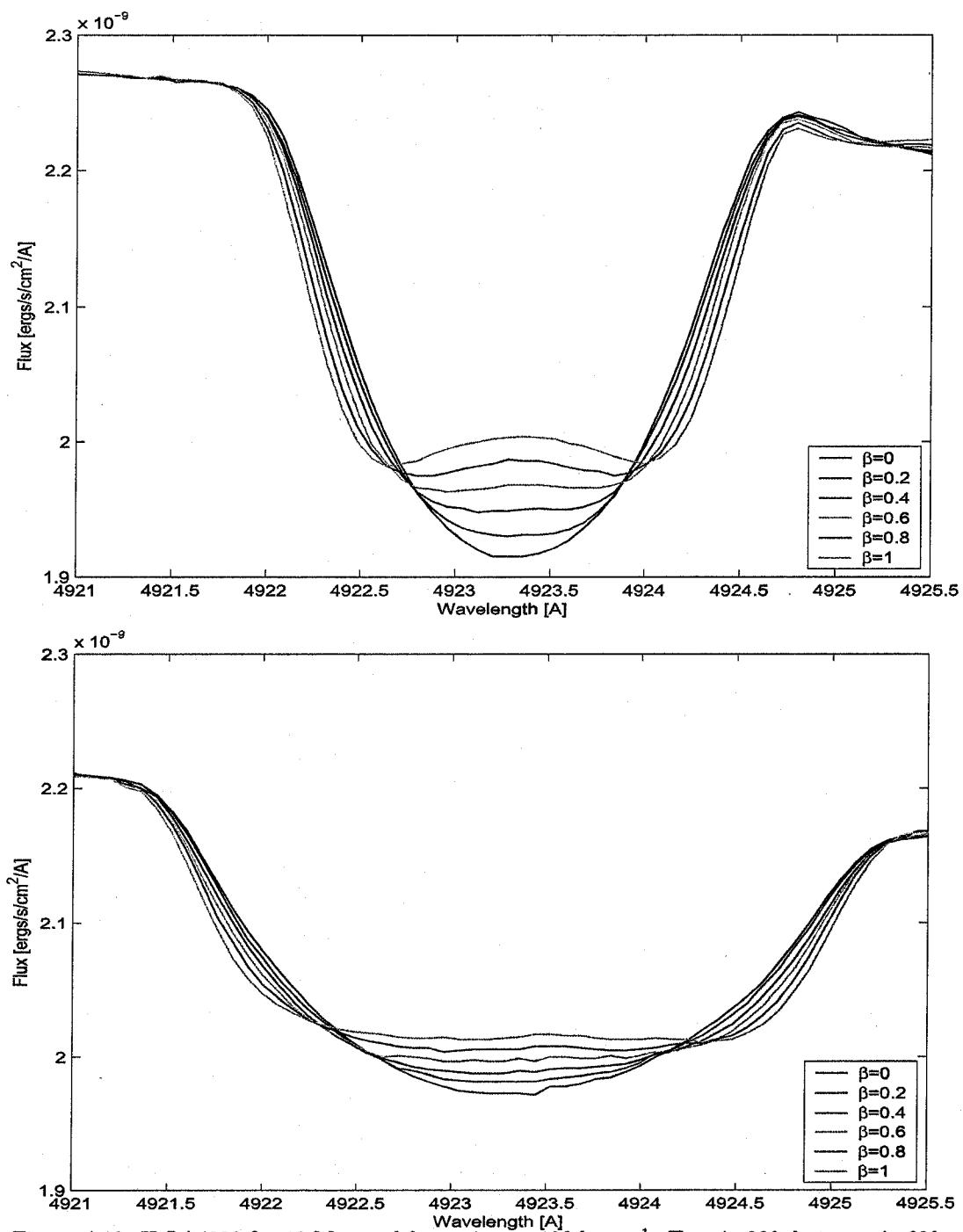


Figure 4.10: He I $\lambda 4923$ for $10 M_\odot$ model rotating at 120 km s^{-1} . Top: $i=30^\circ$, bottom: $i=60^\circ$.

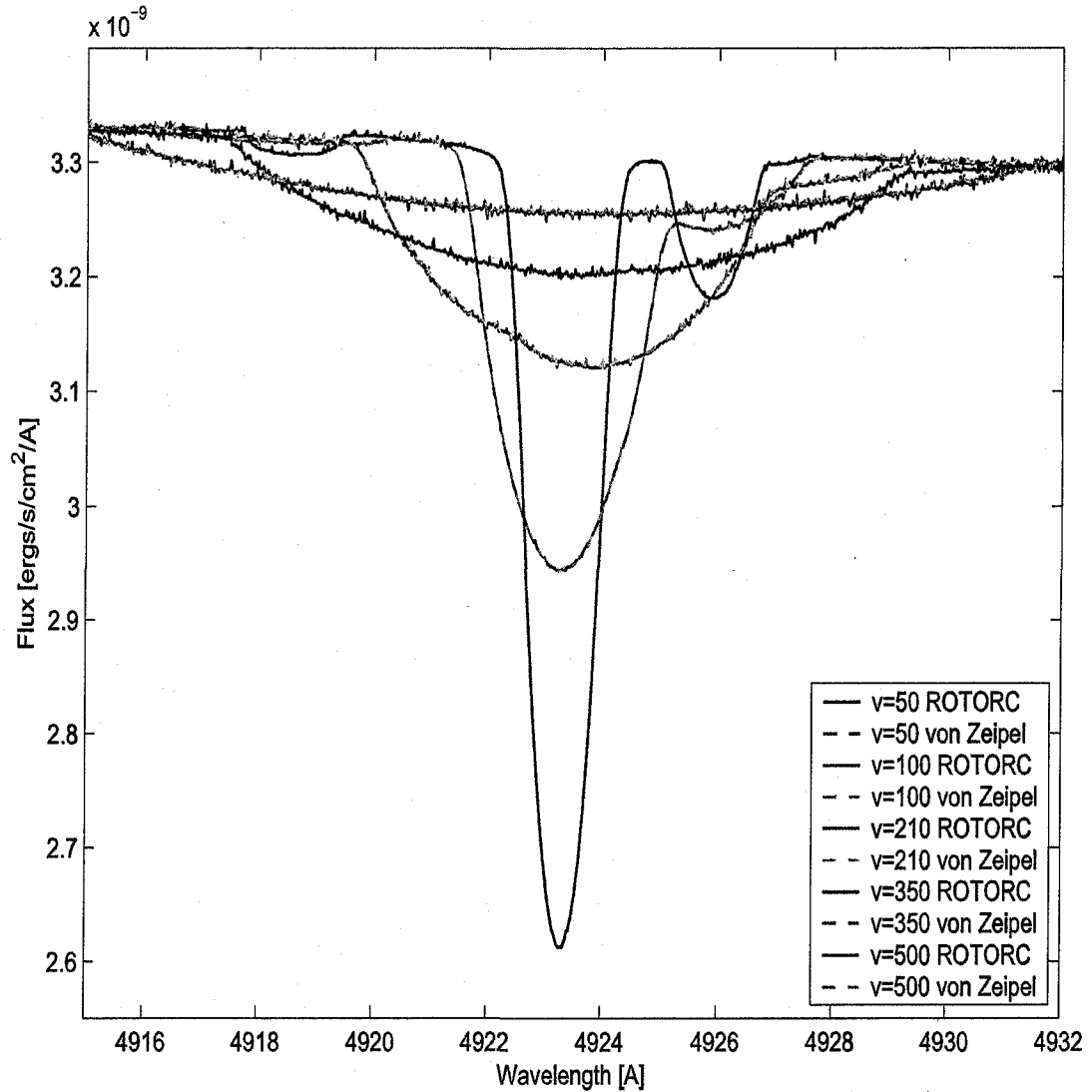


Figure 4.11: He I $\lambda 4923$ generated from ROTORC (solid) and Von Zeipel (dotted) structures for uniformly rotating $12 M_{\odot}$ models viewed equator on.

dotted lines are almost indistinguishable. As seen in the previous chapter, the structural differences between von Zeipel's law and ROTORC are very small for rotational velocities below about 350 km s^{-1} . In the case of He I $\lambda 4923$, for rotational velocities above about 350 km s^{-1} the line is significantly broadened to a degree that it is nearly indistinguishable from the continuum.

Fig. 4.12, which shows the H δ profiles, also shows virtually no discrepancies between the two models at lower rotational velocities, and only slight changes at very high rotational velocities. As mentioned, the only differences that von Zeipel's law makes to the surface structure are in gravity and temperature, which modestly affect the core of the line, but not the broadening. Another result is that the differences only become apparent in the structure at very high rotational velocities. At such velocities, all the weaker lines have been washed out. The only lines left for comparison are some of the stronger lines in either the UV, or the Balmer series. As seen in the previous section, stronger lines do not show much response to subtle changes in the models. In short, while von Zeipel's law fails to match more realistic SED calculations at high rotation, it gives an adequate representation for line profile calculations because all but the strongest lines have already been broadened into near invisibility by rapid rotation.

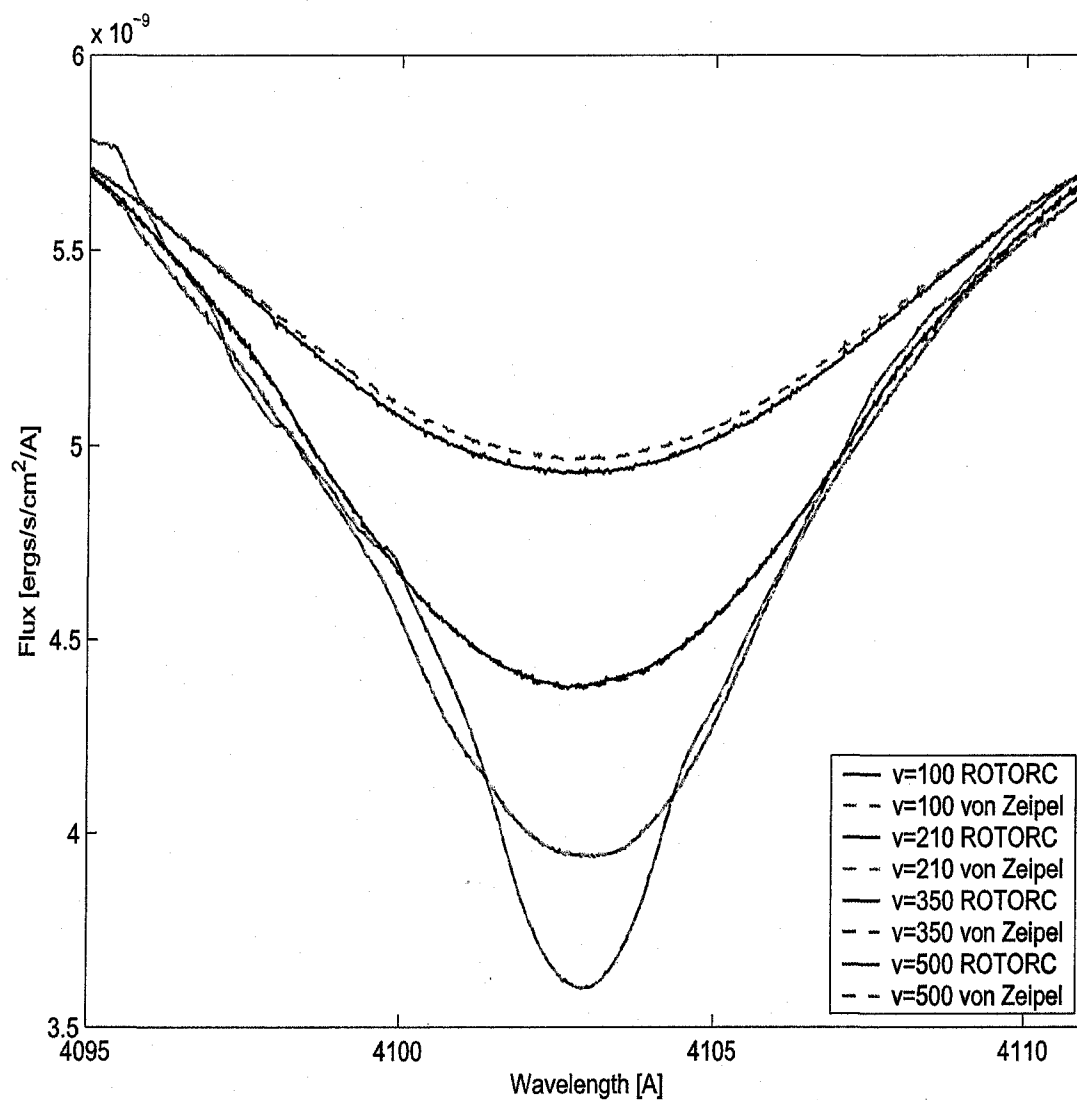


Figure 4.12: H δ generated from ROTORC (solid) and Von Zeipel (dotted) structures for uniformly rotating 12 M $_{\odot}$ models viewed equator on.

CHAPTER 5

CONCLUSIONS

The goal of this work has been to analyze the effects of rapid rotation on SEDs and line profiles. Most of the improvements upon previous studies can be attributed to the more sophisticated modelling tools used. The fully implicit 2D stellar structure code ROTORC was used to generate a series of interior structure models for uniformly and differentially rotating stars. The non-LTE stellar atmosphere and spectrum synthesis code PHOENIX was used to generate a grid of plane-parallel stellar atmospheres. An intensity integrator code, CLIC, was then used to create SEDs and absorption line profiles for a series of rotating stellar models.

The first part of this work focused on using SEDs to define a rotating star's possible locations in the HR diagram. While previous studies have explored the idea, this work introduced the idea of the inclination curve. The primary purpose was to establish a consistent and accurate method of defining the inclination curve that can be repeated and expanded upon in future work. I created a set of inclination curves for $12 M_{\odot}$ models uniformly rotating from 0 to 575 km s^{-1} or near critical rotation. It was found that uniform rotation creates a relatively straight line parallel to the main sequence. The line extended in length and moved away from the main sequence as the rotation rate increased. The results agreed qualitatively with previous studies.

I also created a series of inclination curves for $10 M_{\odot}$ models at 120 and 240 km s^{-1} with varying degrees of differential rotation. The curve was no longer a straight line on the HR diagram, but rather an arc that passed through the main sequence. Increasing the amount of differential rotation had the effect of extending the inclination curve in both the luminosity and the temperature directions. As a result, increasing the amount of differential rotation makes the star appear to be rotating more rapidly.

Inclination curves generated from ROTORC structure models were also compared to structures generated from von Zeipel's law. All other factors, including the grid of atmospheres used, remained the same. The temperature structure of the von Zeipel models began to diverge significantly from the ROTORC models for rotational velocities above $\sim 350 \text{ km s}^{-1}$ or $0.76\omega_c$, where ω_c is the critical rotation velocity. It was around this velocity that the von Zeipel model based inclination curves also diverged from the ROTORC based inclination curves beyond the uncertainties given. It is therefore recommended not to use von Zeipel's law to calculate inclination curves for stars rotating faster than approximately $0.76\omega_c$.

The next part of this work explored the effect of differential rotation on line profiles. Most studies had explored increasing differential rotation or only mild cases of decreasing differential rotation, which often focused on equatorial views with little exploration of other inclination angles.

The combination of tools used in this work allowed the modelling of very strongly decreasing differential rotation, and produced line profiles for a star viewed from any inclination. It was found that the line profiles created by decreasing differential rotation were very distinct from those created by uniform rotation. The equator-on view of the line profiles created by differential rotation were broadened at the wings and had flattened cores. That agrees with the results of previous studies. However, the more intriguing results were found as the observer's line of sight became more pole-on. At low inclinations, the increasingly flattened core of the line became inverted, creating central reversal at the base of the wings.

Such features created very distinctive line profiles for the strongly differentially rotating models. For more mild cases the features were more subtle, but nonetheless present to a degree that is observable with today's telescopes.

Other studies have often found significant differences between uniform and differential rotation in line profiles examined in the Fourier domain. While the differences presented in this thesis were found to be distinctive without the need for a Fourier analysis, it is suggested that the technique be adopted in future work, particularly for finer variations of differential rotation.

Work was also done to test the effects of von Zeipel's law on rotationally broadened line profiles. It was found that, while von Zeipel models have less accurate surface properties and hence inclination curves at high rotation velocities, there is no detectable effect on line profiles. Weaker lines are broadened to a degree that they are nearly indistinguishable from the continuum at rotational velocities of significance, and stronger lines were too broad to be very significantly affected by the differences in structural models.

Rotating stars present us with a myriad of problems that will never be adequately addressed by a single line of research. This work presents some unique new results that illustrate the benefits of a strong collaboration between stellar structure modelling and stellar atmospheres in tackling multidisciplinary problems like rotating stars.

REFERENCES

- Bodenheimer, P. 1971. *ApJ*, 167, 153
- Boehm-Vitense, E. 1981. *ARA&A*, 19, 295
- Brown, P.J.F., Dufton, P.L., Lennon, D.J. & Keenan, F.P. 1986. *MNRAS*, 220, 1003
- Carroll, J.A. 1928. *MNRAS*, 88, 548
- Carroll, J.A. 1933. *MNRAS*, 93, 478
- Clement, M.J. 1974. *ApJ*, 194, 709
- Clement, M.J. 1978. *ApJ*, 222, 967
- Clement, M.J. 1979. *ApJ*, 230, 230
- Collins, G.W. 1963. *ApJ*, 138, 1134
- Collins, G.W. 1965. *ApJ*, 142, 265
- Collins, G.W. 1966. *ApJ*, 146, 914
- Collins, G.W. 1974. *ApJ*, 191, 157
- Collins, G.W. & Harrington, J.P. 1966. *ApJS*, 146, 152
- Collins, G.W. & Smith, R.C. 1985. *MNRAS*, 213, 519
- Collins, G.W. & Sonneborn, G.H. 1977. *ApJS*, 34, 41
- Collins, G.W. & Truax, R.J. 1995. *ApJS*, 439, 860
- Collins, G.W., Truax, R.J., & Cranmer, S.R. 1991. *ApJS*, 77, 541
- Cramer, N. 1984. *A&A*, 132, 283

- Deupree, R.G. 1990. ApJ, 357, 175
- Deupree, R.G. 1995. ApJ, 439, 357
- Donati, J.F. 2003. ASPC, 307, 41
- Elvey, C.T. 1930. ApJ, 71, 221
- Frémat, Y., Zorec, J., Hubert, A.M., & Floquet, M. 2005. A&A, 440, 305
- Garcia-Alegre, M.C., Vazquez, M., & Woehl, H. 1982. A&A, 106, 261
- Gray, D.F. 1977. ApJ, 211, 198
- Hardorp, J. & Strittmatter, P.A. 1968a. ApJ, 151, 1057.
- Hardorp, J. & Strittmatter, P.A. 1968b. ApJ, 153, 465.
- Hauschildt, P.H. and Baron, E., 1999. J. Comp. App. Math., 109, 41
- Huang, S.S. 1961. ApJ, 133, 130
- Jackson, S. 1970. ApJ, 161, 579
- Lanz, T. & Hubeny, I. 2007. ApJS, 169, 83
- Lennon, D.J., Kudritzki, R.P., Becker, S.R., Eber, F., Butler, K. & Groth, H.G. 1990, in A.S.P. Conf. Ser., Vol. 7, Properties of Hot Luminous Stars, ed. C.D. Garmany (San Francisco: ASP), 315
- Lovekin, C.C. *Models of Achernar: Evolution and atmospheres of a rapidly rotating B star*. MSc thesis, St Mary's University (Canada), 2005.
- Lovekin, C.C., Deupree, R.G., & Short, C.I. 2006. ApJ, 643, 460
- Maeder, G. & Peytremann, E. 1970. A&A, 7, 120
- Mihalas, D., & Athay, R.G. 1973. ARA&A, 11, 187

- Ostriker, J.P. & Mark, J.W.-K. 1968. *ApJ*, 151, 1075
- Reiners, A. 2003. *A&A*, 408, 707
- Reiners, A. & Schmitt, J.H.M.M. 2002. *A&A*, 384, 155
- Roxburgh, I.W., Griffith, J.S. & Sweet, P.A. 1965. *ZAp*, 61, 203
- Roxburgh, I.W. & Strittmatter, P.A. 1965. *ZAp*, 63, 15
- Sackmann, I.-J. & Anand, S.P.S. 1970. *ApJ*, 162, 105
- Schou, J. *et al.* 1998. *ApJ*, 505, 390
- Shajn, G. & Struve, O. 1929. *MNRAS*, 89, 222
- Short, C.I., Hauschildt, P.H., & Baron, E., 1999. *ApJ*, 525, 375
- Slettebak, A. 1949. *ApJ*, 110, 498
- Slettebak, A., Kuzma, T.J., & Collins, II, G.W. 1980. *ApJ*, 242, 171
- Smith, R.C. 1971. *MNRAS*, 151, 463
- Stoeckley, T.R. 1968. *MNRAS*, 140, 121
- Stoeckley, T.R. & Buscombe, W. 1987. *MNRAS*, 227, 801
- Sweet, P.A. & Roy, A.E. 1953. *MNRAS*, 113, 701
- Tassoul, Jean-Louis *Theory of Rotating Stars*. Princeton University Press, Princeton, NJ. 1978.
- Thompson, M.J., Christensen-Dalsgaard, J., Miesch, M.S., & Toomre, J. 2003. *ARA&A*, 41, 599
- von Zeipel, H. 1924. *MNRAS*, 84, 665